

# The Backend Processes Evaluation of Poly-Si(O<sub>x</sub>) Solar Cells: From TCO to Metallization

Jing Zhang

Delft University of Technology

# The Backend Processes Evaluation of Poly-Si(O<sub>x</sub>) Solar Cells: From TCO to Metallization

by

**Jing Zhang**

Student Number

---

5214866

Supervisors: Dr. Peyman Taheri Prof.dr. Olindo Isabella  
Daily Supervisors: Dr. Zhirong Yao Dr. Can Han  
Project Duration: Nov. 2021 - Aug. 2022  
Faculty: Material Science & Engineering, 3ME

# Acknowledgment

With my graduation project gradually completed, my master's program at TU Delft is coming to an end. Despite the hardships of studying abroad due to the heavy academic load and the Covid epidemic, the care and help of my friends and teachers have kept me optimistic and calm. I would like to express my gratitude and blessings to the people who have accompanied me and supported me during these two years.

First of all, I would like to thank my daily supervisors, Dr. Zhirong Yao and Dr. Can Han. Still remember their warm welcome and careful guidance when I first joined the laboratory, which gave me the confidence to complete the project independently. I appreciate their supervision of the project in the past months and their help in my life. Then, I would like to thank my supervisor Prof. dr. Olindo Isabella for involving me in the project and for suggesting the direction of the project at the cluster meetings. Also, the thank goes to my advisor at MSE, Dr. Peyman Taheri, for keeping an eye on the progress of my project and handling the processes necessary for graduation.

Next, I would like to express my gratitude to all the people who have helped me in the PVMD group, including Dr. Guangtao Yang, Ir. Yifeng Zhao and Liqi Cao. As well, I want to acknowledge the technical staff of EKL, Martijn Tijssen, Daragh O'Connor, Stefaan Heriman and Engin Ozkol, who were always very patient in answering instrument-related questions and helping me with equipment problems.

I also want to appreciate my friends in lab and in daily life. First of all, I would like to thank Chengli Hou, who helped me to prepare many samples. Then I would like to thank Fabian, Katarina, Mohua, who shared all the interesting things in the lab with me. I also want to say thanks to my colleague in the office, Nida, for always encouraging me and making me feel relaxed. Next, I would like to express my gratitude to my friends in life, Kubra, Ke Xu, Yu Bi, Xinshuo Zhang, Songyan Liu, Xuesong Zhao, for creating many good memories with me and making me feel less lonely in Delft.

Finally, I would like to thank my parents who have always supported me morally and financially. They have backed all my decisions so that I can remain empowered.

*Jing Zhang  
Delft, August 2022*

# Abstract

In recent decades, there has been increasing concern about the impact of climate change on the earth. Various countries are actively developing sustainable energy technologies, of which solar cell is one of the new energy sources with the most attention. This thesis is based on poly – Si(O<sub>x</sub>) cells consisting of SiO<sub>x</sub>/poly – Si(O<sub>x</sub>) passivating contact. Various methods have been investigated to mitigate the TCO (IWO) deposition induced passivation degradation and to optimize the screen printing process.

First, the approaches to reduce the passivation degradation due to IWO deposition were explored. The power density and working pressure in IWO deposition were optimized. With utilizing 1.23 W/cm<sup>2</sup> power density and 5×10<sup>-3</sup> mbar working pressure, the *iV*<sub>OC</sub> degradation was reduced to 4.7 mV for *n*<sup>+</sup> sample (NAOS-SiO<sub>x</sub>) and to 7.9 mV for *p*<sup>+</sup> sample after deposition of 75 nm IWO. Besides, hydrogenated amorphous silicon and AZO were used as buffer layers for the *p*<sup>+</sup> SiO<sub>x</sub>/poly – Si(O<sub>x</sub>) samples, finding that they were effective in reducing sputtering damage. Then, the optimal post-annealing condition was investigated, which turned out to be vacuum annealing at 400 °C for 30 min, recovering the 49 mV and 60 mV *iV*<sub>OC</sub> for *n*<sup>+</sup> sample (thermal-SiO<sub>x</sub>) and *p*<sup>+</sup> sample, respectively. Based on the above experiments, the first cells were prepared with a maximum efficiency of 17.4%.

Second, the existing screen printing process in the lab was optimized. The 0.37% organic solvent was added into the silver paste, reducing the viscosity of paste. The snap-off distance was changed to 0.02 mm in order to improve the continuity of printed grids. Moreover, the squeegee speed was optimized to 30 mm/s, limiting the spreading of silver paste to 57.3 μm, much narrower than the initial spreading distance of 155.3 μm.

Finally, a batch of poly – Si(O<sub>x</sub>) cells were prepared by applying the above various optimized conditions. The cell with optimized IWO and optimized screen printing process performed best with a champion efficiency of 18.9%.

# Contents

<b>Acknowledgment</b>	<b>i</b>
<b>Abstract</b>	<b>ii</b>
<b>Nomenclature</b>	<b>ix</b>
<b>1 Introduction</b>	<b>1</b>
1.1 Background . . . . .	1
1.2 Solar energy technology . . . . .	2
1.2.1 Semiconductor . . . . .	2
1.2.2 Principle of solar cell . . . . .	3
1.2.3 Loss mechanisms in solar cell . . . . .	4
1.3 Passivating contact . . . . .	7
1.4 Motivations . . . . .	8
1.5 Objectives . . . . .	9
1.6 Outline . . . . .	10
<b>2 Fundamentals and experimental</b>	<b>11</b>
2.1 TCO and properties . . . . .	11
2.1.1 TCO . . . . .	11
2.1.2 Electrical property . . . . .	11
2.1.3 Optical property . . . . .	12
2.1.4 Trade-off between electrical and optical properties . . . . .	12
2.2 Sputtering damage . . . . .	13
2.3 Metallization . . . . .	14
2.3.1 Screen printing . . . . .	15
2.3.2 Optimization . . . . .	16
2.4 Experimental . . . . .	16
2.4.1 Sample preparation flowchart . . . . .	16
2.4.2 Process equipments . . . . .	20
2.4.3 Characterization equipment . . . . .	23
<b>3 Passivation degradation mitigation</b>	<b>29</b>
3.1 Introduction . . . . .	29
3.2 Experimental . . . . .	29

---

3.3	Sputtering damage reduction . . . . .	31
3.3.1	Power density optimization . . . . .	31
3.3.2	Working pressure optimization . . . . .	33
3.3.3	Buffer layer for $p^+$ sample . . . . .	34
3.4	Recovery effect enhancement . . . . .	35
3.4.1	Annealing temperature optimization . . . . .	35
3.5	IWO properties . . . . .	35
3.6	Cell performance . . . . .	36
3.6.1	8 nm a-Si:H as buffer layer . . . . .	37
3.6.2	IWO optimization . . . . .	39
3.6.3	The texturing treatment . . . . .	39
3.7	Other improvement . . . . .	40
3.7.1	AZO as buffer . . . . .	40
<b>4</b>	<b>Screen printing optimization</b>	<b>42</b>
4.1	Introduction . . . . .	42
4.2	Experimental . . . . .	42
4.3	Initial screen printing setup . . . . .	43
4.4	Optimized screen printing . . . . .	43
4.4.1	Viscosity of paste . . . . .	44
4.4.2	Snap-off distance . . . . .	46
4.4.3	Squeegee speed . . . . .	46
4.5	Flowchart . . . . .	48
<b>5</b>	<b>Cell fabrication</b>	<b>50</b>
5.1	Introduction . . . . .	50
5.2	Experimental . . . . .	51
5.3	Cell performance . . . . .	52
5.3.1	Screen printing optimization . . . . .	52
5.3.2	The application of buffer layer . . . . .	52
<b>6</b>	<b>Conclusions and outlook</b>	<b>55</b>
6.1	Conclusions . . . . .	55
6.2	Outlook . . . . .	56
6.2.1	TCO-related improvements . . . . .	56
6.2.2	Utilization of copper-plating technique . . . . .	58
6.2.3	Device-related improvements . . . . .	58
	<b>References</b>	<b>59</b>

# List of Figures

1.1	Contribution of each technology to the reduction of CO <sub>2</sub> emissions in the electrical sector between 2016 and 2050 in IEA 2DS vs. 6DS[3]. . . . .	2
1.2	Energy band diagrams of a conductor, semiconductor and insulator[4]. . . . .	3
1.3	The electron-hole pair generation by photon absorption[7] . . . . .	4
1.4	A solar cell with a simple structure includes each step up to the generation of an electric current[5]. (1) An electron-hole pair is created by absorbing photons. (2) The electron and hole recombine.(3) The separation of electrons and holes can be achieved through an interface acting like a semi-permeable membrane. (4) Separated electrons can be used to drive a circuit. (5) Following the passage of the electrons through the circuit, they will recombine with the holes. . . . .	4
1.5	Schematic diagram of the main recombination mechanisms in solar cells[8].	7
1.6	Recombination at semiconductor surface[4]. . . . .	7
1.7	The band diagram of the SiO <sub>x</sub> /poly – Si(O <sub>x</sub> ) passivating contact structure[17]. . . . .	9
1.8	The structure of poly – Si(O <sub>x</sub> ) solar cell. . . . .	9
2.1	The optical performance for a typical TCO material[27]. . . . .	12
2.2	The sputtering process and potential substrate damage mechanisms[16].	14
2.3	The schematic of screen printing machine[5]. . . . .	16
2.4	The flowchart for passivation sample, $p^+$ sample as an example here. . . . .	17
2.5	The flowchart for contact study sample, $p^+$ sample as an example here. . . . .	18
2.6	The flowchart for single-sided textured poly – SiO <sub>x</sub> cell fabrication. . . . .	19
2.7	The scheme for IWO characterization sample. . . . .	20
2.8	The internal structure and components of PECVD[39]. . . . .	21
2.9	The internal structure and components of RF sputtering machine[39]. . . . .	22
2.10	The mechanism of atomic layer deposition (ALD)[41]. . . . .	23
2.11	The difference between classical ALD and spatial ALD[42]. . . . .	23
2.12	The WCT-120 from Sinton Instruments, used for carrier lifetime measurement[44]. . . . .	24
2.13	The digital rotational viscometer[45] . . . . .	26
2.14	the Olympus optical microscopy. . . . .	27

2.15	Left: electrons interact with solids to produce different signals[48] Right: the scanning electron microscopy (Hitachi Regulus 8230). . . . .	28
3.1	The $iV_{OC}$ of $n^+$ (left) and $p^+$ (right) passivation samples before/after 75nm IWO deposition with various sputtering power density (working pressure = $3 \times 10^{-3}$ mbar). . . . .	32
3.2	The lifetime as a function of minority carrier density for a $n^+$ passivation sample before/after 75nm IWO deposition (power density= $1.23\text{W}/\text{cm}^2$ , working pressure = $3 \times 10^{-3}$ mbar). . . . .	32
3.3	The $iV_{OC}$ of $n^+$ (left) and $p^+$ (right) passivation samples before/after 75 nm IWO deposition with various sputtering working pressure (power density = $1.23\text{ W}/\text{cm}^2$ ). . . . .	33
3.4	The structure for $p^+$ passivation sample with a-Si:H as buffer layer. . . . .	34
3.5	The $iV_{OC}$ of $p^+$ passivation samples applied various thickness a-Si:H before/after 75nm IWO deposition. . . . .	34
3.6	The $iV_{OC}$ of $n^+$ (left) and $p^+$ (right) passivation samples after IWO deposition and 30 – min vacuum annealing under various temperature. . . . .	35
3.7	The lifetime as a function of minority carrier density for a $n^+$ passivation sample after IWO deposition and $400\text{ }^\circ\text{C}$ vacuum annealing for 30 mins. . . . .	36
3.8	The first basic structure for poly – $\text{Si}(\text{O}_x)$ cell applied 8 nm a-Si:H as buffer. . . . .	37
3.9	The performance of poly – $\text{Si}(\text{O}_x)$ cells with/without a-Si:H as buffer layer. The values shown are the average based on 5 cells from the same batch. . . . .	38
3.10	The contact resistivity for different samples. . . . .	38
3.11	The performance of poly – $\text{Si}(\text{O}_x)$ cells: with different IWO deposition. The values shown are the average based on 5 cells from the same batch. . . . .	39
3.12	The performance of poly – $\text{Si}(\text{O}_x)$ cells with different texturing treatment. The values shown are the average based on 5 cells from the same batch. . . . .	40
3.13	Left: the $iV_{OC}$ of $p^+$ passivation samples after 20 nm ALD AZO, 60 nm IWO deposition and vacuum annealing Right: the normalized lifetime of $p^+$ passivation samples after deposition of buffer layer (a-Si:H or AZO) & IWO and vacuum annealing. . . . .	41
4.1	The morphology of grid printed under lab conventional screen printing condition. . . . .	43
4.2	The morphology of grid printed with $40\text{ }\mu\text{m}$ opening. . . . .	44
4.3	The viscosity of silver paste as a function of adding organic solvent (weight fraction). . . . .	45

---

4.4	The SEM images for the cross-section of the grids with different weight fraction of organic solvent. . . . .	45
4.5	The image observed by optical microscopy for the grid with 0.37% weight fraction of organic solvent. . . . .	46
4.6	The shape of the printed grids at different snap-off distances. . . . .	47
4.7	The paste spreading width for seven separate sets of grid printed at different velocities. . . . .	47
4.8	The shape of the printed grids at different squeegee speed. . . . .	48
4.9	The SEM image for the cross-section of the grid with 30 mm/s squeegee speed. . . . .	48
4.10	The flowchart for optimized screen printing. . . . .	49
5.1	The structure for poly – Si(O <sub>x</sub> ) cell, with $n^+$ poly – Si(O <sub>x</sub> ) on the front side.	51
5.2	The $J - V$ curve the champion device in this thesis with 18.9% efficiency.	53
5.3	The performance of poly – Si(O <sub>x</sub> ) cells with/without buffer layer. The values shown are the average based on 4 cells from the same batch. . . .	53
6.1	The properties of IWO films prepared under various O <sub>2</sub> fraction. . . . .	57

# List of Tables

2.1	The recipe for different layers deposited by PECVD. . . . .	21
3.1	The properties of optimized IWO. . . . .	36
5.1	The average parameters for the cells applied ref-SP and optimized-SP. The cell area is 4.0 cm <sup>2</sup> . . . . .	52

# Nomenclature

---

Abbreviation (Symbol)	Definition
IEA	International Energy Agency
PERL	Passivated Emitter Rear Locally-diffused Solar Cell
TCO	Transparent Conducting Oxide
ITO	Tin-doped Indium Oxide
IWO	Tungsten-doped Indium Oxide
ALD	Atomic Layer Deposition
a-Si	Amorphous silicon
a-Si:H	Hydrogenated Amorphous Silicon
BHF	Buffered Oxide Etch
c-Si	Crystalline Silicon
$E_g$	Bandgap Energy
$E_{ph}$	Photon Energy
$FF$	Fill Factor
$\eta$	Efficiency
$N_e$	Electron Concentration
$\mu_e$	Electron Mobility
$iV_{OC}$	Implied Open Circuit Voltage
$V_{OC}$	Open Circuit Voltage
$J_{sc}$	Short Circuit Current Density
LPCVD	Low-Pressure Chemical Vapour Deposition
PECVD	Plasma Enhanced Chemical Vapour Deposition
NAOS	Nitric Acid Oxidation of Silicon
rpm	Rotations Per Minute
SEM	Scanning Electron Microscope
SRH	Shockley-Read-Hall
TMA	Trimethylaluminium
TMAH	Trimethyl Ammonium Hydroxide

---

# 1

## Introduction

### 1.1. Background

The human evolution to social development has led to the necessity of changing the surroundings for meeting the growing demands. Attempting to do so, human beings trended to congregate in particular areas which offered the greatest comfort. The exponential growth of population within such defined areas has produced large-scale urban areas full of commerce, industry and business[1]. While this might be seen as a positive fact, it has also brought numerous consequences related to pollution and harmful emissions, which have been proven to have an impact on the current climate.

Climate change has been an extensively discussed topic for decades. During the last few centuries, its influence has increased dramatically, leading to issues including population redistribution, species endangerment, agriculture-related problems, and ecosystem degradation[1]. Thankfully, there is an increasing awareness of the problem and various solutions have been proposed, such as the shifting of fossil fuel use to more "eco-friendly" sources.

Carbon dioxide (CO<sub>2</sub>) levels in the atmosphere have increased by 45% since humans began burning fossil fuels on a massive scale in the late 19<sup>th</sup> century[2]. CO<sub>2</sub> is a well-known greenhouse gas that absorbs infrared radiation and contributes to the warming of the earth. In June 2016, the International Energy Agency (IEA) published *Energy Technology Perspectives 2016: Towards Sustainable Urban Energy Systems*[3], which predicted global warming in the coming decades. The worst-case scenario for climate change, if nothing is done, is a 6 °C (6DS) increase in global average temperature compared to pre-industrial levels. Comparatively, the target is an increase of up to 2 °C (2DS), requiring a large-scale shift from fossil fuels to carbon-free energy sources as early as possible.

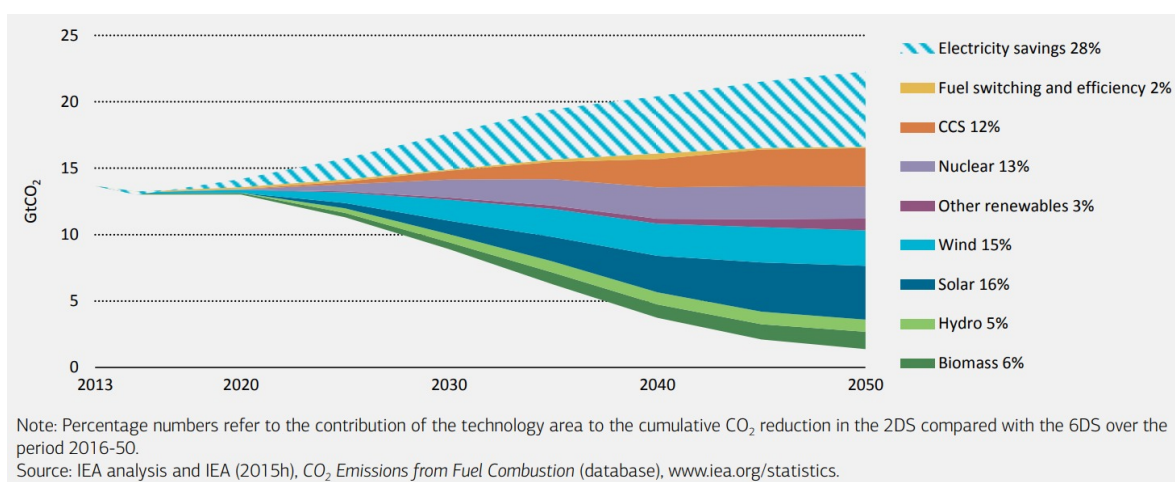


**Figure 1.1:** Contribution of each technology to the reduction of CO<sub>2</sub> emissions in the electrical sector between 2016 and 2050 in IEA 2DS vs. 6DS[3].

Figure 1.1 presents IEA's estimate of the CO<sub>2</sub> emission reductions (cumulative from 2016 to 2050) required to realize the 2DS, in the electricity sector[3]. Of this, 28% comes from electricity savings, which comes primarily from energy efficiency improvements in electricity use, 45% from renewables, and the remaining 27% from nuclear power and carbon capture & storage. Remarkably, solar energy accounts for 16% and is the largest contributor to CO<sub>2</sub> reduction among renewable energy sources. It can be said that the development of solar energy technology is extremely important for reducing CO<sub>2</sub> emissions, achieving the 2DS target and curbing climate change.

## 1.2. Solar energy technology

### 1.2.1. Semiconductor

Semiconductor is the basic material used in solar cell devices, e.g., silicon. Semiconductor is defined relative to conductors and insulators, therefore, it can be identified by measuring the conductivity. Metals are typically conductive materials (i.e., conductors) and the conductivity ( $\sigma$ ) can be greater than  $10^3$  S/cm, while that of insulators (e.g., glass) is less than  $10^{-8}$  S/cm; semiconductors have a broad conductivity range that lies between these two extremes[4].

Energy band theory can explain the difference between conductors, semiconductors and insulators more intuitively, as shown in Figure 1.2[4]. In a conductor, the conduction and valence bands overlap, no band gap exists, allowing electrons to move freely without hindrance. Hence, it has an excellent electrical conductivity. Whereas in an insulator, where the valence electrons are tightly bound around the atom, the thermal energy required for the valence electrons to gain freedom is excessively high and difficult to achieve. Insulators therefore have a very high resistivity. In between, in a semiconductor, although the valence electrons cannot move freely, they are able to

escape from the atomic binding with a narrower energy gap: if an external source can provide a certain amount of energy ( $>$  bandgap energy), the electrons can move to the conduction band and leave a hole in valence band.

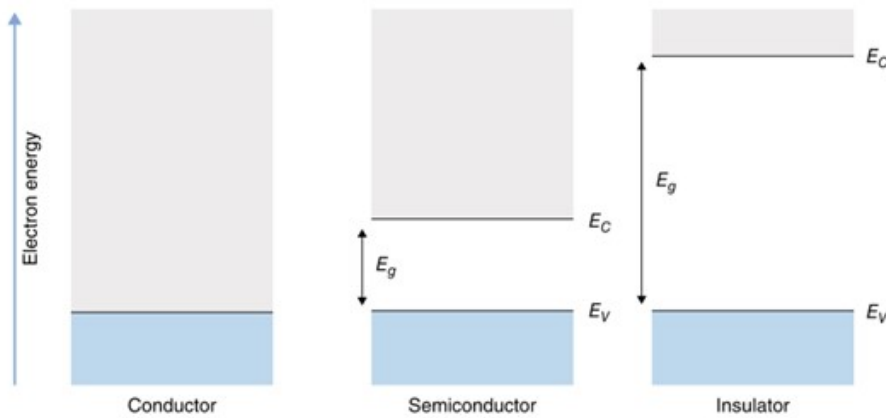


Figure 1.2: Energy band diagrams of a conductor, semiconductor and insulator[4].

### 1.2.2. Principle of solar cell

The photovoltaic effect is the working principle of solar cells, where a potential difference is created at the junction of two different materials in response to electromagnetic radiation[5]. The photovoltaic effect can be divided into three basic processes: generation, separation and collection of charge carriers.

- Charge carriers generation by the photon absorption  
In the previous section (1.2.1), it has been mentioned that electron-hole pairs can be generated when energy is supplied to the semiconductor from an external source. For photovoltaic, sunlight is the main energy source. When a semiconductor absorbs a photon, as shown in Figure 1.3, the radiative energy it carries will be used to excite the electron in the valence band, leaving a hole in the valence band[6]. Principally, photons of energy higher than the bandgap of the absorber material will produce electron-hole pairs, the so-called charge carriers.
- Photo-generated charge carrier separation  
This step is essential, otherwise the electron-hole pairs will recombine, i.e., the electrons will drop back to the valence band, like (3) in Figure 1.4. We need an interface that acts like a semi-permeable membrane, allowing one type of carrier to pass and blocking the other. In most solar cells, n-type and p-type semiconductors serve this purpose ( placed on each side of the absorber).

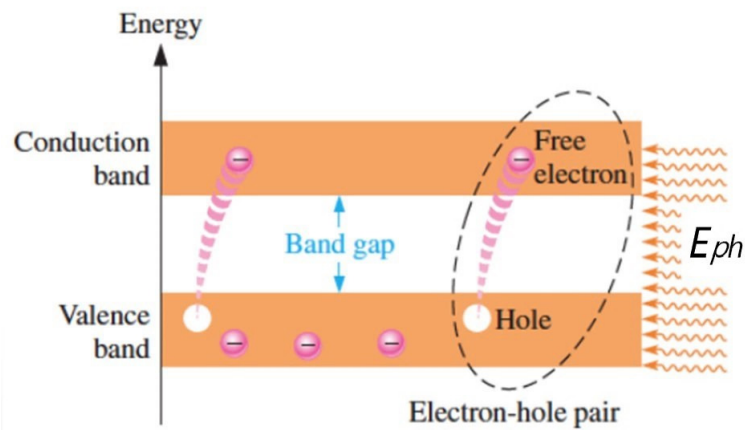


Figure 1.3: The electron-hole pair generation by photon absorption[7]

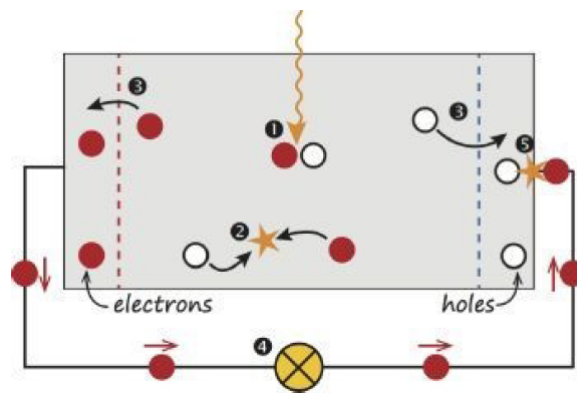


Figure 1.4: A solar cell with a simple structure includes each step up to the generation of an electric current[5]. (1) An electron-hole pair is created by absorbing photons. (2) The electron and hole recombine. (3) The separation of electrons and holes can be achieved through an interface acting like a semi-permeable membrane. (4) Separated electrons can be used to drive a circuit. (5) Following the passage of the electrons through the circuit, they will recombine with the holes.

- Collection of photo-generated charge carriers by terminals

An external circuit is connected to the two ends of a solar cell to form a complete current path. The electrons are extracted at one end, travel through the external circuit, and eventually recombine with holes at the other end, corresponding to the (4)(5) in Figure 1.4.

### 1.2.3. Loss mechanisms in solar cell

Solar cell efficiency in crystalline silicon is limited by three loss mechanisms: optical loss, electrical loss and recombination loss (collection loss)[5].

#### Optical loss

- Thermalization and non-absorption

When the incident photon is carrying an energy higher than the bandgap of the material, an electron-hole pair will be created. The excess energy will be

lost and released in the semiconductor material as heat. This is referred to as "thermalization". Conversely, if the energy carried by the photon is below the material bandgap, the semiconductor will not be able to absorb that energy, which is known as non-absorption.

- Reflection loss

One would expect the incident photons to be absorbed as much as possible by the absorbing layer, but this is unrealistic. For example, some of the incident photons will be reflected before reaching the absorber layer, resulting in reflection loss.

- Parasitic absorption

If photons are absorbed in a layer other than the absorber (e.g. a conductive oxide layer) the phenomenon is called parasitic absorption. This absorption does not contribute to the generation of charge carriers.

- Shading loss

In most c-Si solar cells, thin metal strips are placed on the front side of the solar cell to serve as front electrodes. The area covered by the metal does not allow light to enter the solar cell, but reflects or absorbs the incident light, and the resulting loss is called shading loss.

### Electrical loss

- Resistive loss

In solar cells, the bulk resistance of the junctions, the contact resistance between the junctions and the electrodes, and the resistance of the electrodes themselves are not negligible. They can cause the voltage generated by the solar cell as well as the  $FF$  to drop.

- Shunt loss

When the current passes through a local defect in the junction or the shunt at the solar cell edge is not suppressed, a leakage current will be generated. This also leads to a decrease in cell voltage and in  $FF$ .

### Recombination loss

Carrier recombination at the surface of body parts, interfaces and junctions can seriously affect the charge carrier collection. An excessively high recombination rate is detrimental to the performance of the cell as it leads to a reduction in carrier lifetime and transport efficiency. Recombination can be divided into bulk recombination and

surface recombination[8].

There are three main types of bulk recombination: radiative recombination (band-to-band recombination), Auger recombination, and trap-assisted recombination (SRH).

- Radiative recombination

Radiative recombination is the recombination of electrons in the conduction band with holes in the valence band, resulting in the emission of a photon at the band gap energy  $E_g$ . The nature of the semiconductor material determines the radiative recombination, where the coefficient is much larger in direct bandgap materials than in indirect bandgap materials. Therefore, in indirect bandgap materials, such as crystalline silicon, radiative recombination usually does not have a dominant role.

- Auger recombination

Auger recombination is a non-radiative process. Different from radiative recombination, the energy of its photogenerated carriers is not dissipated by photon emission, but transferred to a third particle. For example, two electron collisions can lead to the recombination of electron and hole, leading to the release of energy. This energy is then converted into kinetic energy for the remaining electron and eventually dissipated through a thermalization process.

- Shockley–Read–Hall recombination

Impurities or vacancies at a certain concentration are unavoidable in semiconductors, and they lead to spatially localized defect levels within the semiconductor bandgap ( $E_t$  in the figure), which are capable of trapping free carriers (hence often referred to as trap states). Such trap-assisted non-radiative recombination is the predominant recombination mechanism in most solar cells, where the trapped energy is released in the form of phonons.

As shown in the Figure 1.6, the dangling unpassivated bonds and the absorbed impurity molecules on the surface of the solar cell can generate a very high density of trap states. These trap states can be regarded as an infinite source of carrier recombination, since their distribution over the band gap is almost continuous[9]. Without passivation, these surface traps can cause severe losses to the cell, which is the so-called surface recombination.

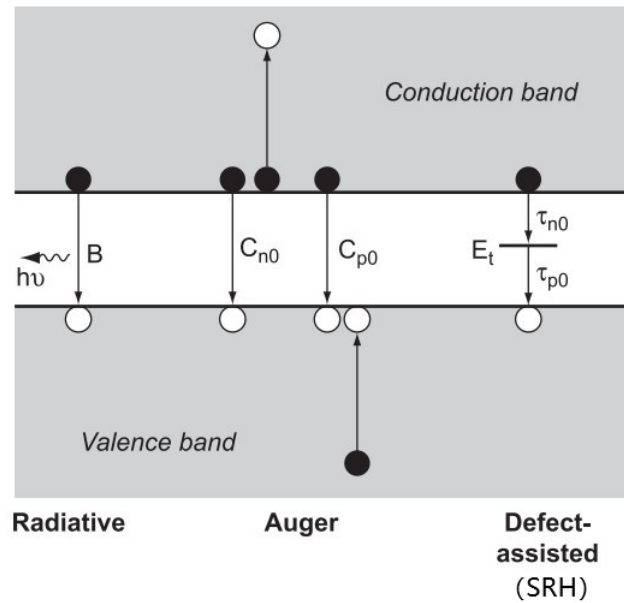


Figure 1.5: Schematic diagram of the main recombination mechanisms in solar cells[8].

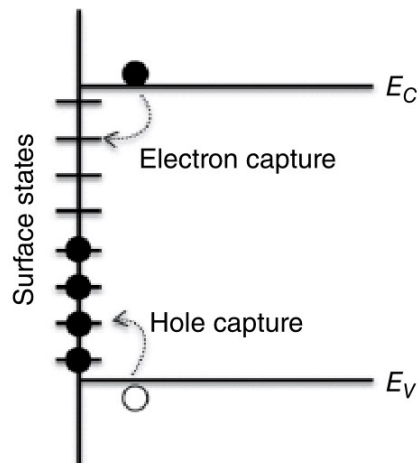


Figure 1.6: Recombination at semiconductor surface[4].

### 1.3. Passivating contact

As previously introduced in Section 1.2.2, a metal contact is required for a solar cell to extract the generated carriers from the device. Nevertheless, direct contact at metal-semiconductor interfaces results in a quasi-continuous defect distribution in the semiconductor bandgap, leading to severe recombination (Section 1.2.3). The conventional approach to reduce recombination rates is to introduce highly doped regions, which will reduce the number of minority carriers at the interface and thus suppress recombination. However, inevitable increases in Auger recombination are caused by such highly doped regions, which ultimately limit the efficiency of silicon solar cells.

In parallel, efforts had been made by scientists to minimize the metallization region and to strictly limit the highly doped zone to the metallization region. These attempts enables PERL cell with localized contacts to have 25% efficiency and maintained the highest record for several years[10]. But, even though the percentage of metallized area in such cells is less than 1%, these metal-semiconductor interfaces still drive unacceptable recombination rates[11].

Another way to avoid severe surface recombination is to make this metal-silicon contact disappear: removing silicon and metal is impractical, but inserting a layer of something else between the two seems feasible. This is the inspiration for the passivating contact, a structure that is currently receiving unparalleled attention. The name suggests that passivating contacts have surface passivation and contact functions. An ideal passivating contact minimizes charge carrier recombination losses at the interface, simultaneously allowing efficient charges extraction from the semiconductor with external circuits. Thus, similar to a semipermeable membrane, the passivating contact is selective according to the type of carrier, i.e., the conductivity of one carrier type ( $e^-$  or  $h^+$ ) must be much better than another carrier type. Otherwise, the majority and minority carriers will recombine at the electrodes if they are extracted with the same possibility[12]. In recent years, the single junction silicon solar cells with efficiencies over 25% all feature passivating contact, demonstrating its great potential, and flexibility compatibility in structural design[13].

## 1.4. Motivations

The  $\text{SiO}_x/\text{poly} - \text{Si}(\text{O}_x)$  passivating contact is one of the passivating contacts, as shown in the Figure 1.7. Here, a layer of tunnel oxide ( $\text{SiO}_x$ ) is inserted between c-Si and poly -  $\text{Si}(\text{O}_x)$ [14]. It avoids direct contact between semiconductor and metal, reducing recombination losses, as introduced in Section 1.3. Meanwhile, the  $\text{SiO}_x$  provides chemical passivation for the c-Si and prevents the diffusion of dopants from poly -  $\text{Si}(\text{O}_x)$ . Moreover, the doped poly -  $\text{Si}(\text{O}_x)$  offers the field-effect passivation.

Our project is based on a structure shown in Figure 1.8, where both sides of solar cell apply the  $\text{SiO}_x/\text{poly} - \text{Si}(\text{O}_x)$  passivating contact. In the following, this cell is referred to as the poly -  $\text{Si}(\text{O}_x)$  solar cell. Therefore, the poly -  $\text{Si}(\text{O}_x)$  layer cannot be deposited too thick (no more than 20 nm), otherwise it would introduce severe parasitic absorption and affect the optical performance. However, such thin poly -  $\text{Si}(\text{O}_x)$  has very high sheet resistance (above  $1000 \Omega \text{ sq}^{-1}$ ). Hence, a highly conductive and transparent TCO is needed to assist the charge carrier transport to the metal grid[15]. Here, the TCO used is IWO. For the next metallization step, screen printing is chosen as it is the method widely used in the industry.

Nevertheless, in order to fabricate poly – Si(O<sub>x</sub>) cell with excellent performance, we need to first solve two well-known technical challenges.

The first challenge is the sputtering damage induced during the TCO deposition. The bond dissociation energy of Si-Si and Si-H bonds is about 3 eV, while particles such as plasma generated during sputtering carry energy of no less than 10 eV[16]. Therefore, a large number of defects, such as dangling bonds, can arise on the silicon surface, leading to passivation degradation.

The second challenge is the trade-off of the metallization step. The front surface electrodes reduce the effective area of the solar cell, which results in shading losses[5]. Hence it is desirable to keep the area covered by the grid small enough, but this causes a large series resistance. Consequently, the optimal metallization is a compromise between a small coverage area and a sufficiently low series resistance.

If we can find an effective way to deal with these two difficulties, it is then able to produce poly – Si(O<sub>x</sub>) cells with excellent properties.

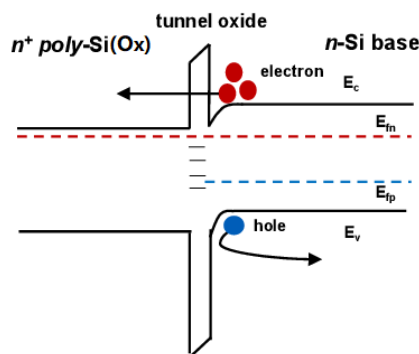


Figure 1.7: The band diagram of the SiO<sub>x</sub>/poly – Si(O<sub>x</sub>) passivating contact structure[17].

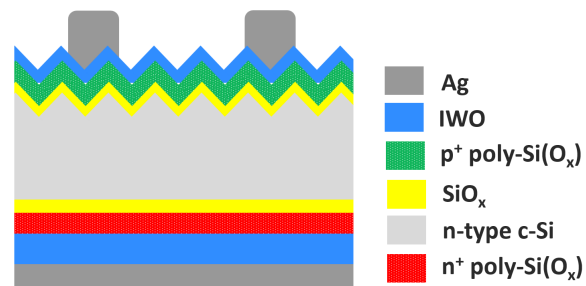


Figure 1.8: The structure of poly – Si(O<sub>x</sub>) solar cell.

## 1.5. Objectives

Based on the motivation mentioned above, we can divide the objectives of this project into the following three points. **First, to reduce passivation degradation due to TCO deposition.** This can be achieved both by reducing sputtering damage as well as by enhancing passivation recovery. **Second, to optimize the existing screen printing.** In order to reduce masking losses, the grids should be narrow sufficiently. For compensating the high series resistance associated with a narrow grid, the grid is supposed to be thick enough. Therefore, basically, the finger height should be as high

as possible, while the finger width should be as small as possible to comply with these requirements. **Finally, on the basis of the optimization described above, prepare the poly – Si(O<sub>x</sub>) solar cell.**

## 1.6. Outline

**This thesis is outlined in the following manner:**

Chapter 1: Introduction. This chapter provides an overview of the climate change crisis and the worldwide emphasis on the development of new energy sources (especially photovoltaics). Also, the working principle and loss mechanism of solar cells are presented. Next, the structure and advantages of passivating contact are explained, as well as the challenges faced by poly – Si(O<sub>x</sub>) cells. This is followed by the research objectives of this thesis project.

Chapter 2: Fundamentals and Experimental. The fundamentals of TCO, the origin of sputtering damage, and the principles of screen printing are discussed in this chapter. A detailed description of the passivation samples, contact samples, and cell preparation processes involved is given. Also, the various process equipment and characterization techniques used in this thesis are introduced.

Chapter 3: Passivation degradation mitigation. The approaches to reduce the passivation degradation due to IWO deposition are explored, including adjusting the IWO recipe, adding buffer layer, optimizing annealing temperature. A cell with 17.4% efficiency is fabricated based on these optimizations.

Chapter 4: Screen printing optimization. This chapter introduces the optimization on the screen printing. The relation between paste viscosity and adding solvent is presented. And the effect of snap-off distance and squeegee speed on the printing quality is studied. Finally, the grid lines painted by the 40 μm width screen are obtained, which have a three-dimensional shape and good continuity.

Chapter 5: Cell fabrication. A batch of poly – Si(O<sub>x</sub>) cells are prepared by applying the above various optimized conditions. The cell with optimized IWO and screen printing process performs best with a champion efficiency of 18.9%.

Chapter 6: Conclusions and outlook. This chapter summarizes the important results of this thesis and gives the outlook.

# 2

## Fundamentals and experimental

### 2.1. TCO and properties

#### 2.1.1. TCO

TCO is the abbreviation for transparent conducting oxide, who can help solar cells to collect charge carriers and guide incident light simultaneously. In detail, the TCO distributed in front of the solar cell acts as an optically transparent electrode, transmitting incident light to the active layer and transporting photogenerated electrons to the terminals of external devices to form a current loop, thereby improving the efficiency of the solar cell. Based on these two main functions, the requirements for suitable TCO materials for photovoltaic devices can be deduced: excellent electrical conductivity & optical transparency.

The present mainstream TCO is indium-based ( $\text{In}_2\text{O}_3$ ) materials, whose bandgap is 2.9 eV [18]. There are many choices of dopants suitable for  $\text{In}_2\text{O}_3$ , including Ti[19], Ce[20], Mo[21], W[22], etc. The most common one is ITO, tin-doped indium oxide. Tin tin impurities replace the indium ions in the  $\text{In}_2\text{O}_3$  lattice in the ITO crystal. If the tin impurities are oxidized, electrons will escape into the conduction band of ITO, resulting in an increase of carrier density in the conduction band, thereby improving the conductivity [23]. Researchers have demonstrated long ago the excellent overall properties of ITO: high transparency, low resistivity, outstanding adhesion to metal contacts & substrates, and more absorption in the long wavelength region[24]. However, tungsten-doped indium oxide (IWO) exhibits better mobility at high temperatures and higher transmittance in the near-infrared wavelength region[25]. Therefore, IWO was chosen to be used in this project.

#### 2.1.2. Electrical property

Considering the band gap of TCO is usually larger than 3 eV, it is difficult for the intrinsic material to excite electron and hole pairs. So the electrical conductivity of

TCO materials mainly comes from internal defects (oxygen vacancies and interstitial) or external dopants. The solubility of the dopants limits the carrier concentration of TCO, which varies from  $10^{20}$  to  $10^{21}$   $\text{cm}^{-3}$ . As for mobility ( $\mu_e$ ), another factor related to conductivity, it is limited by lattice scattering. Numerous electron scattering mechanisms have been identified by scientists, including ionized impurities, neutral centers, thermal vibrations of crystal lattices, structural defects, and grain boundaries. The carrier concentration and crystal quality inside the TCO will largely determine the scattering mechanism[26]. Generally, the resistivity of TCO is about  $10^{-4}$   $\Omega$  cm.

### 2.1.3. Optical property

The optical performance of a typical TCO is shown in Figure 2.1[27]. This spectrum can be divided into three segments to explain the optical properties of TCO. In the high-energy short-wavelength part, the absorption fraction is high. As the wavelength increases to the active region of the absorber, the energy provided by incident photons is lower than the bandgap energy of the TCO, indicating satisfactory transparency. After a broad highly transmissive wavelength band, the absorption increases again, which is the so-called free carrier absorption. It can be explained with the Drude model of metals that was developed by Paul Drude in 1900[28].

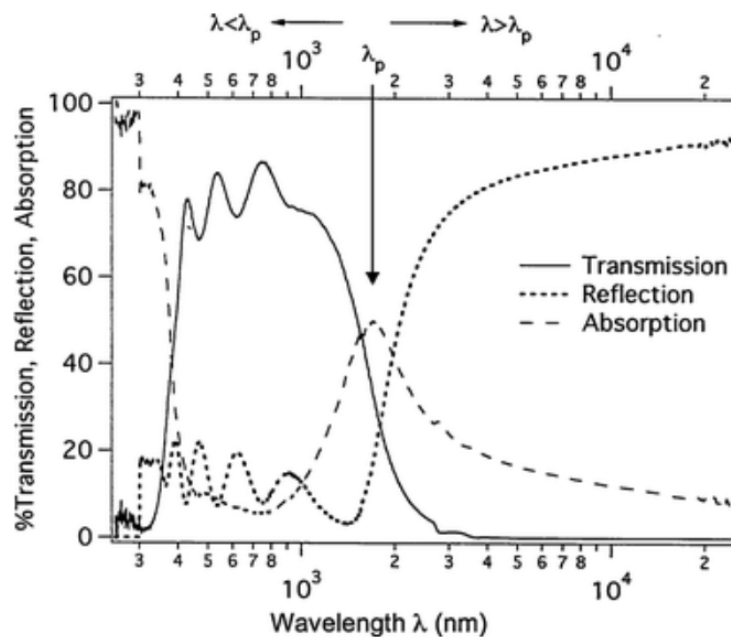


Figure 2.1: The optical performance for a typical TCO material[27].

### 2.1.4. Trade-off between electrical and optical properties

For a qualified transparent conducting oxide (TCO) for photovoltaic applications, it should have the following properties[29]:

- (1) Low lateral resistivity**
- (2) Low contact resistance with adjacent layers**
- (3) Low light absorption loss in the solar cell operating band**
- (4) Limited sputtering damage to passivation**
- (5) Appropriate refractive index for maximum light in-coupling**

These requirements involve two essential values: carrier concentration ( $N_e$ ) and electron mobility ( $\mu_e$ ). Although the carrier transport between the TCO and the adjacent active layer is positively correlated with the carrier density, if the carrier density is too high, it will lead to severe free carrier absorption in the near-infrared region[29]. On the other hand, considering the formula for conductivity ( $\sigma = e\mu_e N_e$ ), it is not difficult to find that high electron mobility can compensate for the loss of conductivity caused by low carrier concentration. Therefore, improving the electron mobility of TCO has become the research direction of scientists.

## 2.2. Sputtering damage

Whether for laboratory research or industrial production, magnetron sputtering is the most common method for preparing TCO. This technique ignites a gas (usually Ar) with direct current or radio frequency energy source, exciting the plasma. High-energy plasma particles are generated to bombard the target, transferring of the target particles to the substrate to form a dense film, as indicated in Figure 2.2. During this process, the sensitive layers of the device, such as the passivation layer, may be damaged by the high kinetic energy of the plasma particles, the light emitted by the plasma, and the heat generated by processing. As a result, the device's performance and stability will be affected[16].

The bombardment of substrates by high-energy particles is the leading cause of sputtering damage, including ions generated in plasma (15-20 eV), negative ions on the target surface (400 eV) and the sputtered atoms or ions from the target surface (10 eV)[30]. The energy required for hydrogen to bind to a crystalline silicon surface or an amorphous silicon substrate is about 3.25 eV, much lower than that associated with the particles mentioned above. As a result, the Si-H bond is easily broken during the TCO deposition process, failing the original passivation, increasing defect density. At the same time, the substrate temperature increases during deposition, potentially triggering physical or thermal degradation of sensitive substrate layers. These phenomena will lead to the degradation of solar cell performance. Therefore, it is critical to slow down or eliminate the sputter damage that occurs during TCO deposition.

One way to reduce sputtering damage is adjusting the deposition process. Investiga-

tions focusing on different parameters were conducted, including sputtering power[31], sputtering methods[32], and the magnetic field strength[33], etc. Another method is to apply post-annealing to restore the passivation, and the selected annealing temperature will affect the recovery effect significantly[31].

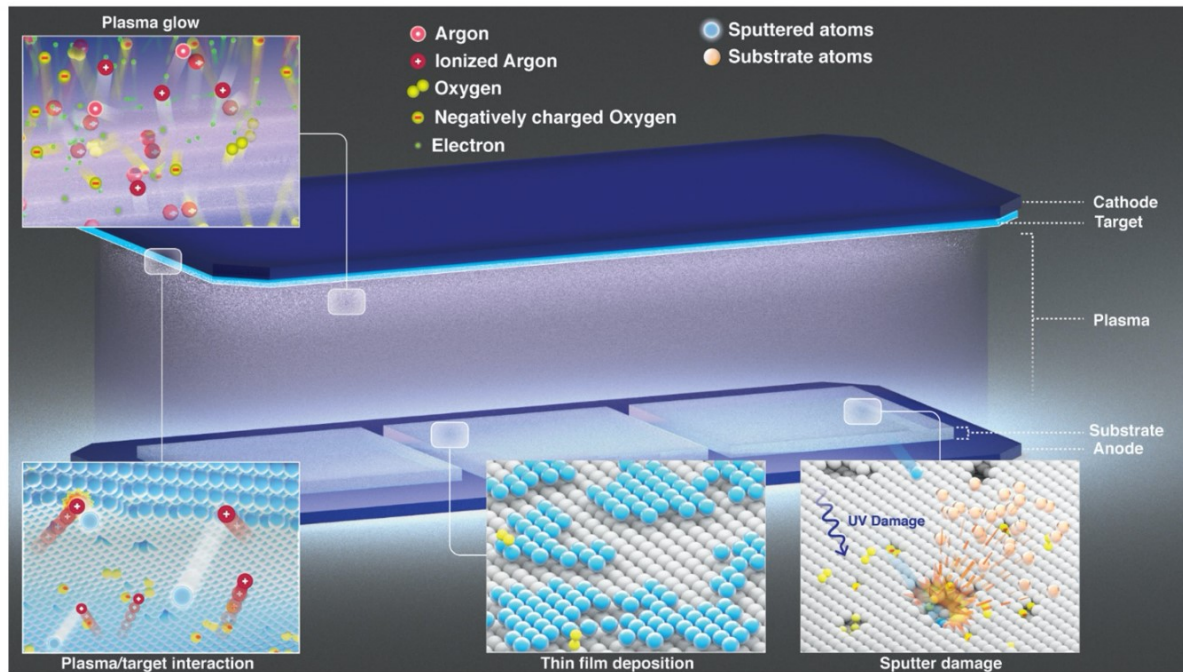


Figure 2.2: The sputtering process and potential substrate damage mechanisms[16].

### 2.3. Metallization

Metallization is critical part of the solar cell fabrication process, because the current generated from illumination is delivered to the external circuit through the metal electrodes. The design and quality of metallization can largely determine the final performance of the cell.

The electrodes of a monofacial solar cell are typically composed by a front electrode and a back electrode[5]. The front electrode faces the sun and is generally an H-shaped structure that includes fine grids and main grids. Fine grids are used to collect the current, while the main grids aggregate the current from the fine grids to the external circuit. The rear electrode is commonly metallized with a full area and is relatively simple. As described in the previous section, screen printing is currently the most popular method for metallization of solar cells in industry due to its affordability and consistent quality. In this project, the front and rear electrodes were first printed on the cell by screen printing, then dried to remove the organic solvent in the paste, and cured to make real contact between the electrodes and the wafer, finally realizing

the establishment of the current transmission channel.

However, metallization also brings additional losses to the cell, which include four main aspects: recombination loss, shading loss, and series loss. Recombination loss, as the name implies, is the loss of efficiency due to the additional recombination. For cells featuring with passivating contacts, even though the direct contact between the metal and the crystalline silicon has been eliminated, some metal particles may still pass through the TCO, poly – SiO<sub>x</sub> and SiO<sub>x</sub> layers and reach the crystalline silicon surface after metallization, leading to an aggravation of local recombination. Shading loss is the reduction of active area due to the presence of front grids that cover the solar cell[5]. This part of the metal-covered area does not allow light to penetrate, but reflects or slightly absorbs the incident light. So in terms of shading loss, the narrower the grids, the better. Nevertheless, a narrow grid can lead to additional series losses (the lateral resistance and the grid resistance become larger). Therefore, the compromise between shading loss and series loss of the front electrode is essential: the typical solution is to increase the aspect ratio of the grid (small width, large height). In this thesis, we mainly focus on the shading loss minimization.

### 2.3.1. Screen printing

The most dominant metallization method in the industry today is screen printing, which accounts for about 97% of the share[4]. Compared to other metallization methods, the advantages of screen printing are apparent. First advantage of screen printing is its simplicity. Next, there is a high designability of screen patterns: in theory, it is possible to achieve any shape and pattern by screen printing. The third point is the low resistivity of silver and the low contact resistance with silicon after high temperature curing. Meanwhile, screen printing has been used for a long time to produce solar cells on a large scale, which suggests that no additional investment in equipment is required. With these characteristics, screen printing remains the leading technology for large-scale manufacturing of solar cells.

The metallic source in screen printing is a liquid present as a viscous paste. Three basic structures are included in a screen printer, as illustrated in the Figure 2.3: a frame, a screen and a squeegee. Following the installation of the screen and squeegee onto the frame, a suitable amount of silver paste needs to be placed under the squeegee. There is no direct contact between the silicon wafer and the screen at this time. Once the parameters are set, the squeegee will move at a constant speed and simultaneously apply a pressure to force the metallic paste through the screen openings. Eventually, the squeegee returns to its original position and the wafer is released, leaving the metallic grid above the wafer[5].

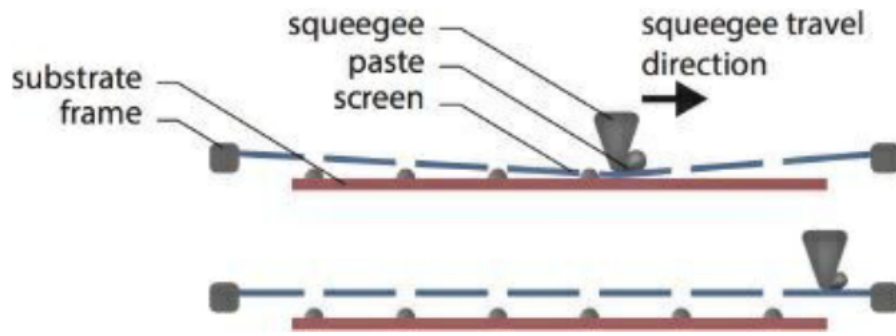


Figure 2.3: The schematic of screen printing machine[5].

### 2.3.2. Optimization

There are many parameters that can be adjusted throughout the screen printing process, such as paste viscosity, snap-off distance and squeegee movement speed. Viscosity influences the ease of passing the paste through the screen opening and shaping, while snap-off distance affects the amount of paste falling and the width of the silver spreading. The squeegee speed determines the paste solidifying time of the, thereby deciding the printing completeness and the spreading width of the paste. Detailed experiments are described in Chapter 4.

## 2.4. Experimental

### 2.4.1. Sample preparation flowchart

In this thesis, there are three main types of samples, namely passivation sample, contact sample and solar cell (precursor). The functions and preparation processes of each of the three samples are explained in this subsection.

#### Passivation sample

Passivation sample is used to examine the change in the properties after TCO deposition. The  $p^+$  sample is used as an example to illustrate in Figure 2.4 (the only difference in the  $n^+$  sample is the  $n^+$  doping of poly - Si(O<sub>x</sub>)).

In this thesis, all samples were fabricated using n-type 4-inch high-purity floating zone (FZ) as the substrate for device fabrication so that the effects of metallic impurities and crystal defects could be excluded[34]. Thickness was 280  $\mu\text{m}$  and orientation was (100).

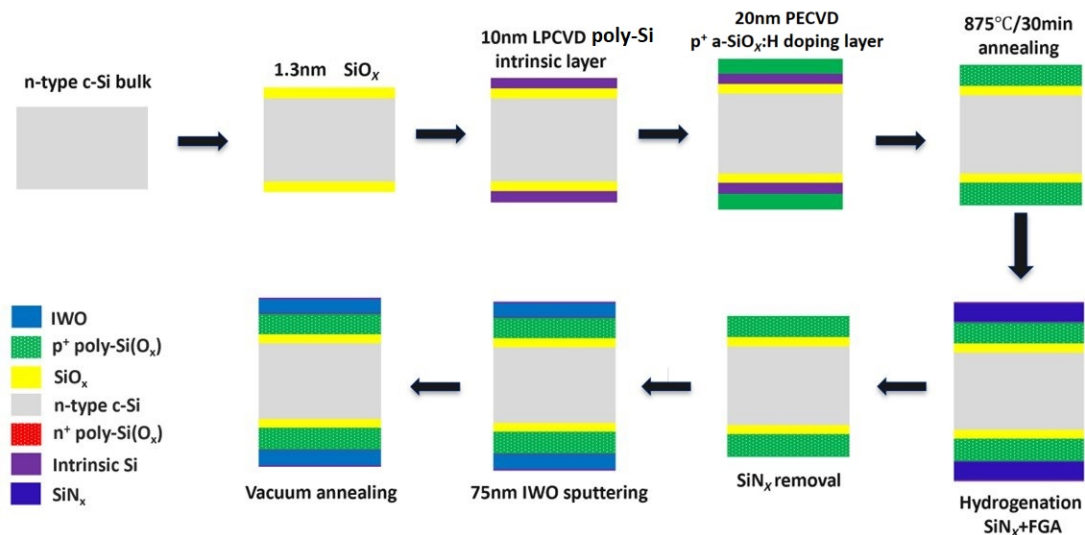


Figure 2.4: The flowchart for passivation sample,  $p^+$  sample as an example here.

Before depositing the silicon oxide, there were several essential cleaning steps (cleaning steps are not indicated in the figure). First, two ten-minute nitric acid soaks were performed in order to remove organic and inorganic contaminants: 99% HNO<sub>3</sub> (@RT) and 69.5% HNO<sub>3</sub> (@110°C), respectively. This was followed by a four-minute immersion in 0.55% HF for the removal of the surface oxide layer, a step that can also be accomplished with the Marangoni. Once all cleaning steps were completed, 1.3 nm interfacial tunneling silicon oxide layer was obtained by two methods. One was to carry a dry thermal oxidation process in a TEMPRESS tube furnace. In the dry thermal oxidation procedure, a constant nitrogen flow rate and oxygen flow rate of 6.00 slm and 0.60 slm were applied at a temperature of 675 °C for 3 minutes. The other method for SiO<sub>x</sub> formation was the nitric acid oxidation of silicon (NAOS). The silicon wafer was immersed into a 69.5% HNO<sub>3</sub> at room temperature for 60 minutes, forming an oxide layer at the surface. Next, 10 nm hydrogenated intrinsic poly-Si and 20 nm boron doped a – Si(O<sub>x</sub>) : H were separately deposited onto the silicon wafer by LPCVD and PECVD. Subsequent annealing returned to the Tempress furnace at a temperature of 875 °C for 30 minutes. Upon completion of annealing, the amorphous layer (a – SiO<sub>x</sub>) would be activated and crystallized into polycrystalline layer (poly – SiO<sub>x</sub>). To supplement the hydrogen lost in the last annealing step and improve the passivation quality, a 75 nm hydrogen-rich SiN<sub>x</sub> layer was deposited by PECVD. Immediately afterwards, a forming gas annealing (FGA) step was conducted to help diffuse the hydrogen into the crystalline silicon bulk to passivate the defects. Up to this point, the sample at the beginning of the experiment was obtained without any parameter adjustment relevant to this thesis.

The next comes the main part of our experiment. Subsequent to hydrogenation, the  $\text{SiN}_x$  layer was etched with BHF and 0.55% HF solution and the properties of the sample were measured as the initial values before the TCO layer deposition. Then a 75 nm IWO was deposited onto both sides of the sample, which was done by RF sputtering. The optimization of the IWO sputtering recipe is discussed in detail in the next sections. After completing the sputtering, the sample properties, such as the minority lifetime, were measured again. Finally, the sputtering damage was repaired and the performance of the IWO was optimized by post-annealing, which is, of course, necessary for the measurement of the sample. An additional note is that we also tried the deposition of an additional buffer layer to reduce the sputtering damage in partial experiments; this buffer layer was done before the IWO deposition and is not indicated in the Figure 2.4.

### Contact sample

The  $p^+$  sample is again employed to demonstrate the procedure for contact sample preparation, shown in Figure 2.5. The flow of contact sample and passivation sample preparation is quite similar, including steps such as cleaning and deposition of silicon oxide, but there are still a few differences. First, to avoid the formation of P-N junctions, the wafer of the  $p^+$  contact sample was a p-type and not n-type. Moreover, after IWO deposition and post-annealing, 500 nm of Ag was evaporated to both sides of the sample.

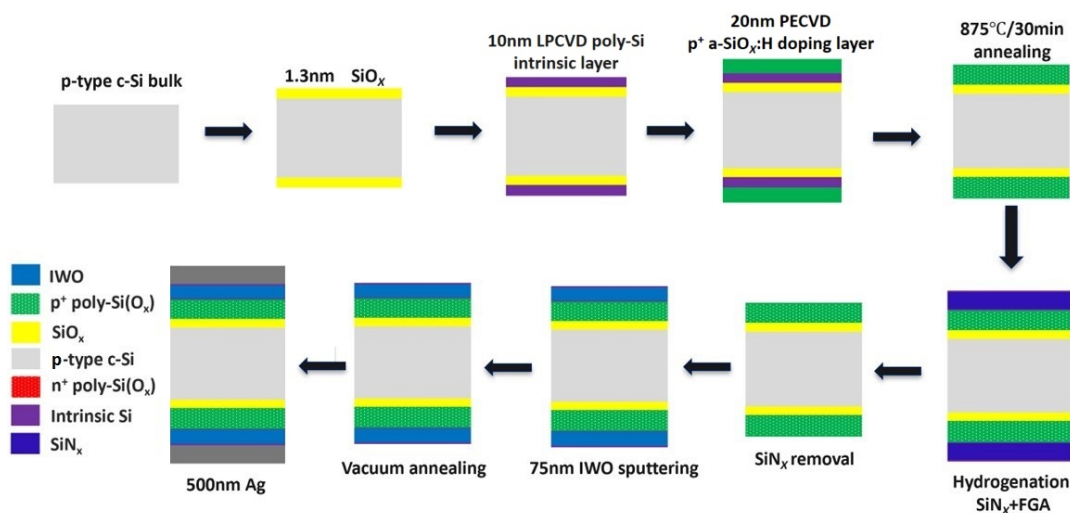


Figure 2.5: The flowchart for contact study sample,  $p^+$  sample as an example here.

### Solar cell fabrication

The solar cell fabrication may involve texturing, as indicated in Figure 2.6. This step was normally done in is the first stage. 105 g of KOH was dissolved in 5 liters deionized

water and heated to 82°C by water bath. Once the solution was prepared, the wafer was immersed for 8 minutes with the addition of a specific organic additive (monoTEX H 2.4). Immediately after texturing, the wafer needed to be rinsed in a hydrochloric acid (HCl) bath to remove the KOH residue. The HCl concentration was 0.20% and was made from 25 ml of 40% HCl dissolved in 5 liters of deionized water. Finally, it was rinsed with water for 5 minutes. In addition, the cell precursor was not a symmetric structure where the doping of the poly – Si(O<sub>x</sub>) on the front side and the back side was different. The shown sample was placed with  $p^+$  poly – Si(O<sub>x</sub>) on the front side and  $n^+$  on the back side, which was fabricated in Section 3.6. And the  $p^+$  poly – Si(O<sub>x</sub>) was deposited on rear side in the last batch of solar cell, as described in Section 5.2. The next annealing and hydrogenation steps were performed in the same way as the preparation of the passivation sample. To obtain a light reflection minimum of about 600 nm by destructive interference effects, which is the peak wavelength of the solar standard spectral irradiance, the front side TCO thickness was restricted to 75 nm (geometry factor of 1.42) for the cell sample[35]. For the rear side, TCO was 150 nm[36]. After deposition of IWO, annealing and metallization were performed. Eventually, there would be 4 or 5 blocks of cells with the same area (4.0 cm<sup>2</sup>) on the wafer (depending on the hard mask used for TCO deposition and metallization), which were independent of each other. The cell performance values were averaged over all cells.

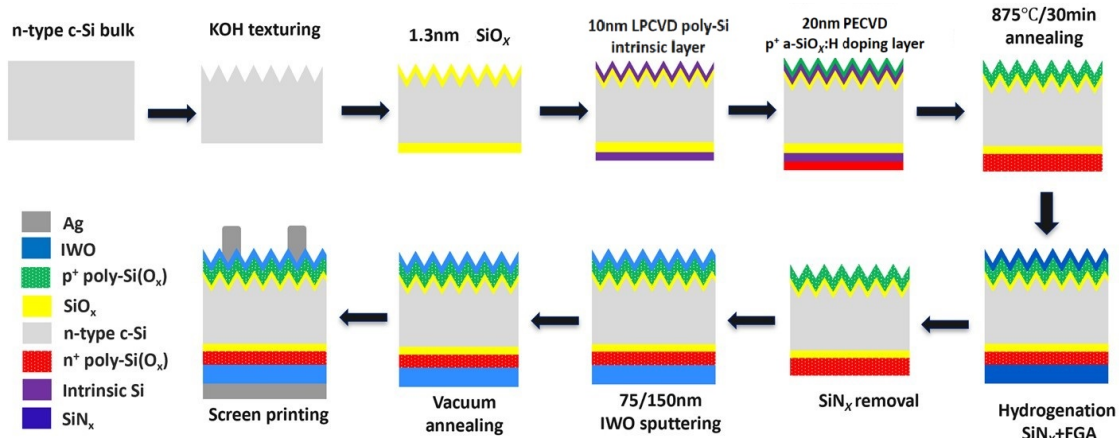


Figure 2.6: The flowchart for single-sided textured poly – SiO<sub>x</sub> cell fabrication.

### IWO characterization sample

For characterization of the IWO properties, 75 nm IWO film was deposited on a Corning glass substrate, as shown in Figure 2.7. The Corning glass sheet had a geometry of 10 cm × 10 cm × 0.7 mm. And it was cleaned in acetone and isopropyl alcohol ultrasonic bath for 10 min before sputtering, respectively.



Figure 2.7: The scheme for IWO characterization sample.

### 2.4.2. Process equipments

#### Low pressure chemical vapor deposition (LPCVD)

In this project, 10 nm intrinsic amorphous silicon films were obtained by LPCVD. This technique has the features of low pressure and long deposition time, and deposited films are pure, high uniformity, and more dense[37]. The equipment is a modular horizontal furnace manufactured by Tempres Systems in EKL100[38]. After the chamber air pressure reaches a specific value, the temperature starts to increase for the reactant gases to start decomposing. The reactant gas used for the deposition of the intrinsic amorphous silicon layer is silane ( $\text{SiH}_4$ ), which is disintegrated into silicon and hydrogen. During the deposition process, the temperature and pressure of the system are maintained at 580 °C and 150 mTorr. At this condition, the deposition rate is approximately 2.2 nm/min. Following deposition, the wafer is annealed at 600 °C for 60 minutes to eliminate any stresses generated on the deposited layer.

#### Plasma-enhanced chemical vapor deposition (PECVD)

Typically, the growth of thin film layers using chemical vapor deposition (CVD) requires temperatures above 600°C to break the chemical bonds of the precursor reactant gases[39]. However, in PECVD (shown in Figure 2.8), the temperature for dissociation of the precursor gas can be significantly lower, between 200 and 400 °C. This is due to the use of plasma in PECVD, where high-energy free electrons and ions provide the necessary energy to break the chemical bonds. The specific process is: a fast alternating electric field between two electrodes ignites the plasma, causing atoms and/or molecules to ionize. These ionized particles carrying high energy collide with gas molecules and initiate the chemical reaction. Deposited layers formed by PECVD are generally of high quality, with good uniformity and desirable thickness. Therefore, PECVD is one of the most popular deposition techniques for manufacturing in the solar cell industry[5].

In this thesis project, PECVD was used several times in the fabrication of various sample species. Two different PECVD devices were used. First, AMOR, manufactured

by Elettrorava, was used to deposit doped a-SiO<sub>x</sub>:H and a-Si:H layers on the wafer surface. The recipes used are shown in Table 2.1. Prior to deposition, the wafer was required to be preheated for at least 15 minutes to reach a stable 180 °C. Deposition of the  $p^+$  dopant layer was conducted in chamber 1, while the  $n^+$  was done in chamber 2. In addition, wafer flipping can be performed in chamber 5.

Another PECVD machine was the Plasmalab 80Plus made by Oxford Systems and located in the Kavli laboratory. It was primarily used to deposit silicon nitride (SiN<sub>x</sub>) layers in the hydrogenation step. The gases used in this deposition were silane (SiH<sub>4</sub>) and ammonia (NH<sub>3</sub>) with 400 degrees Celsius. The equipment was also employed to conduct the subsequent vacuum annealing.

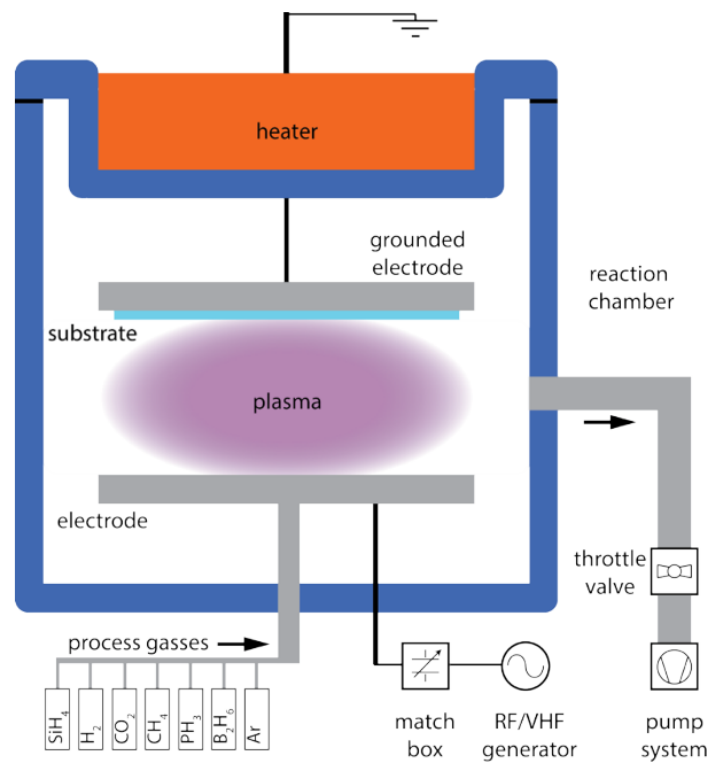


Figure 2.8: The internal structure and components of PECVD[39].

Table 2.1: The recipe for different layers deposited by PECVD.

Layer	Rate (nm/s)	Power (W)	Pressure (mbar)	SiH <sub>4</sub> (sccm)	CO <sub>2</sub> (sccm)	B <sub>2</sub> H <sub>6</sub> (sccm)	PH <sub>3</sub> (sccm)	H <sub>2</sub> (sccm)
$p^+$ a – SiO <sub>x</sub> : H	0.0538	5	2.0	8.0	5.0	20.0	–	100.0
$n^+$ a – SiO <sub>x</sub> : H	0.147	5	1.0	4.0	6.4	–	4.8	35.0
$p^+$ a – Si : H	0.148	5	2.0	8.0	2.5	20.0	–	100.0

### RF sputtering

It has been briefly mentioned the common deposition method for TCO in Section 2.2: magnetron sputtering. This is a physical vapor deposition (PVD) technique[5]. Accelerated ions or atoms bombard the target, transferring energy and momentum, causing the atoms on the target to escape and turn into a gas phase that evaporates. The TCO deposition in this paper was carried out with Zorro, a radio frequency (RF) sputtering machine developed by Polyteknik, as detailed in the Figure 2.9. In the Chapter 3 we have adjusted the sputtering recipe for IWO, and the specific parameters are listed in the Section 3.2.

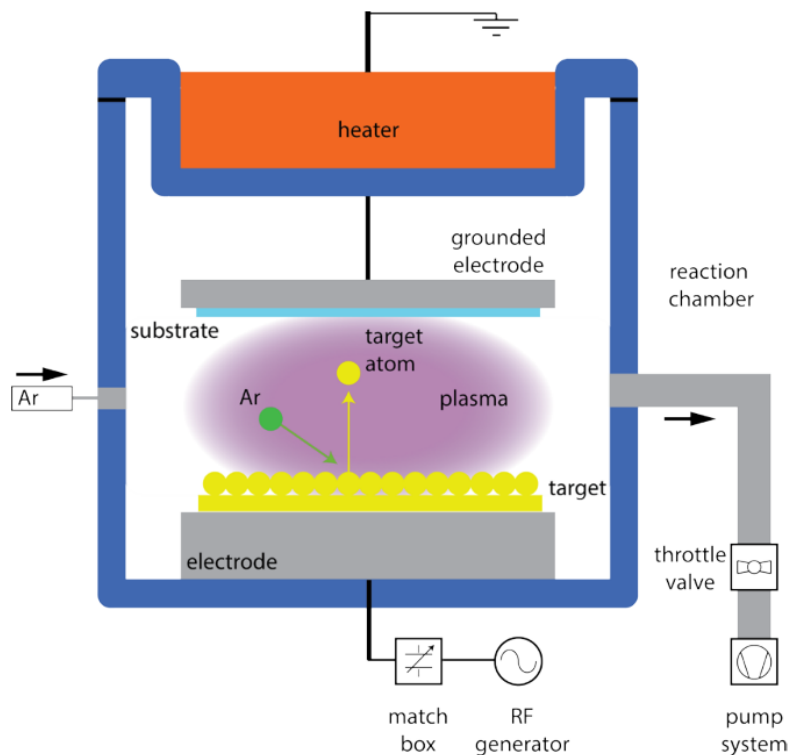


Figure 2.9: The internal structure and components of RF sputtering machine[39].

### Spatial ALD

The ALD technology is reliant on the alternating pulses of precursor gases & vapors on the substrate surface as well as the subsequent chemisorption or surface reaction of the precursors[40]. It is actually a cycle of multiple steps, repeated a certain number of times depending on the desired deposition thickness[41]. The ALD of  $\text{Al}_2\text{O}_3$  is illustrated as an example, involving  $\text{Al}(\text{CH}_3)_3$ , TMA and  $\text{O}_2$  plasma. The substrate is first dosed with the precursor vapor of TMA, which adsorbs and reacts with the surface. This is followed by a clean of all residual precursors and reaction products, as shown in (2). The surface is then exposed to low-damage remote plasma with



from Sinton Instruments, as shown in Figure 2.12.

The total recombination ( $J_{ph}$ ) of the sample with thickness  $W$  can be represented



Figure 2.12: The WCT-120 from Sinton Instruments, used for carrier lifetime measurement[44].

by the average excess minority carrier density  $\Delta n_{av}$  and the effective minority carrier lifetime  $\tau_{eff}$ .

$$J_{ph} = \frac{\Delta n_{av} \cdot q \cdot W}{\tau_{eff}} \quad (2.1)$$

When the silicon wafer is under a steady-state illumination, the densities of photogenerated excess electrons and holes are identical ( $\Delta n = \Delta p$ ). Hence, the excess conductivity  $\sigma_L$  can be stated as ( $\mu_n$  and  $\mu_p$  are the mobility for electron and hole):

$$\sigma_L = q \cdot W \cdot (\Delta n \cdot \mu_n + \Delta p \cdot \mu_p) \quad (2.2)$$

$$= q \cdot W \cdot \Delta n \cdot (\mu_n + \mu_p) \quad (2.3)$$

The carrier lifetime can be calculated in following steps:

$$\Delta n_{av} \cdot q \cdot W = \frac{\sigma_L}{\mu_n + \mu_p} \quad (2.4)$$

$$\tau_{eff} = \frac{\Delta n_{av} \cdot q \cdot W}{J_{ph}} \quad (2.5)$$

$$= \frac{\sigma_L}{J_{ph} \cdot (\mu_n + \mu_p)} \quad (2.6)$$

Therefore, the lifetime is related to the excess conductivity of the sample after illumination.

The lifetime measurement can also yield an implied open-circuit voltage ( $iV_{OC}$ ) curve,

which is equivalent to the  $I - V$  curve for each stage of the solar cell process. This is the most frequently used property in this thesis, which is strongly associated with passivation quality.

### J-V curve measurement

The AAA Wacom WXS-90S-L2 solar simulator was utilized in this thesis to obtain  $I - V$  curve measurements of solar cells. The measurements by Wacom were performed under standard test conditions (STC) with the measurement bench moderately controlled at 25°C. The illumination applied for the measurements consisted of an Xe lamp and a halogen lamp with an irradiance of 1000 W/m<sup>2</sup>. 4-point probe measurements were taken where two probe lines were designed to supply the voltage and the other two probe lines to collect the current.

Several important parameters can be obtained from this measurement[5]:

- Short-circuit current density ( $J_{SC}$ )

$I_{SC}$  is the current obtained by short-circuiting the solar cell externally, without additional load. To eliminate the dependence of  $I_{SC}$  on the solar cell area, however, it is divided by the area to obtain the short-circuit current density ( $J_{SC}$ ). The short-circuit current density is directly related to the incoming illumination, since each absorbed photon produces an electron-hole pair.

- Open-circuit Voltage ( $V_{OC}$ )

The voltage generated by the solar cell without external connections, as expressed in the following equation:

$$V_{OC} = \frac{nkT}{q} \ln\left(\frac{I_{SC}}{I_0} + 1\right) \quad (2.7)$$

where  $n$  is the ideality factor (indicating the degree of ideality of the solar cell),  $kT/q$  is the thermal voltage,  $I_{SC}$  is the short-circuit current mentioned above, and  $I_0$  is the reverse saturation current. The internal reorganization of the solar cell determines the reverse saturation current, which can vary by several orders of magnitude between solar cell devices of different qualities.

- Fill factor ( $FF$ )

it is defined as the ratio between the maximum power produced by the solar cell and the product of the short-circuit current ( $I_{SC}$ ) and the open-circuit voltage ( $V_{OC}$ ), i.e:

$$FF = \frac{I_{mpp} \cdot V_{mpp}}{I_{SC} \cdot V_{OC}} \quad (2.8)$$

where MPP is the operating point at which the solar cell generates the maximum power.  $FF$  can indicate the losses that exist inside the cell. In case  $V_{mpp}$  is

significantly lower than  $V_{OC}$ , a non-negligible series resistance exists somewhere inside the cell, aggravating the recombination. If the difference between  $I_{mpp}$  and  $I_{SC}$  is large, it means that the current does not flow all the way to the external load, i.e., the shunt resistance of the cell is insufficiently high.

- Conversion efficiency ( $\eta$ )

The most important parameter of a solar cell. It represents the ratio between the electrical energy produced by the solar cell and the energy of the incident light, reflecting the ability of the cell to convert light to electricity.

$$\eta = \frac{I_{SC} \cdot V_{OC} \cdot FF}{A \cdot P_{in}} = \frac{J_{mpp} \cdot V_{mpp}}{P_{in}} \quad (2.9)$$

where  $A$  is the area of solar cell and  $P_{in}$  is the incident light power.

### Viscometer

The viscosity of the screen printing silver paste was measured by a digital rotational viscometer, located in the sample preparation room of the ESP basement. As shown in Figure 2.13, this rotating viscometer has a speed-adjustable spindle. Depending on the viscosity of the measured fluid, there are several models of spindles to choose from. It also requires to fix the rotor speed for accurate comparison of viscosity variations. When measuring the viscosity of a particular fluid, after setting the rotation speed, the spindle should be fully immersed in the fluid and the viscosity will be calculated by evaluating the shear between the spindle and the fluid. In this experiment, the selected spindle model was #95 with a rotational speed of 10 rpm.



Figure 2.13: The digital rotational viscometer[45]

### Optical microscopy

The morphology of the grid printed by screen printing was observed by an optical microscope (Microscope Olympus in EKL100). The optical microscope uses a system involving visible light and lenses to magnify the specimen, as illustrated in Figure 2.14[46]. Initially, the image was captured by photographic film, but it has been gradually replaced by digital capture performed by a CCD camera.



Figure 2.14: the Olympus optical microscopy.

### Scanning electron microscopy (SEM)

Since the development of scanning electron microscopy in the early 1950s, it has played a significant role in the academic world[47]. This is because scanning electron microscope has many advantages over traditional optical microscope, such as large depth of field and high resolution. And it allows researchers to better control the magnification as SEM uses an electromagnet rather than a lens. The cross-section of the grids after screen printing in this paper was taken by SEM (Hitachi Regulus 8230 in EKL100).

SEM generates images by scanning the sample with a high-energy electron beam[46]. As shown in the Figure 2.15, when electrons interact with the sample, they produce secondary electrons, backscattered electrons and characteristic X-rays. Once the signals have been collected by the detector, images are formed, which then appear on a

computer screen, as shown at right.



**Figure 2.15:** Left: electrons interact with solids to produce different signals[48]  
Right: the scanning electron microscopy (Hitachi Regulus 8230).

# 3

## Passivation degradation mitigation

### 3.1. Introduction

As mentioned in Section 2.2, the high-energy particles, light and heat generated during TCO sputtering can cause damage to the cell, leading to passivation degradation and lower cell efficiency. For poly – Si(O<sub>x</sub>) cells, a certain thickness of TCO needs to be deposited on both sides of the cell (75 nm on the front surface and 150 nm on the rear surface). Therefore, the passivation degradation induced by TCO deposition needs to be effectively suppressed and mitigated to fabricate a cell with excellent performance.

Two thoughts are typically applied to reduce passivation degradation: reducing the damage caused during deposition[49, 50], and enhancing the passivation recovery effect of post-annealing[31]. In this chapter, different attempts are also carried out along these two directions. We tried to reduce the damage by optimizing the power density and the total air pressure during IWO sputtering, as well as by inserting a buffer layer. Meanwhile, the passivation recovery brought by vacuum annealing was investigated, and the annealing temperature was optimized. In addition, the properties of the IWO itself were characterized.

### 3.2. Experimental

- Sputtering damage reduction

The reference recipe (ref-IWO) parameters for sputtered IWO were: Argon flow rate of 13 sccm, 1%O<sub>2</sub> – 99%Ar flow rate of 7 sccm, substrate temperature of 25 °C, chamber pressure of 4×10<sup>-3</sup> mbar, and power density of 0.55 W/cm<sup>2</sup>. These conditions yielded an IWO deposition rate of 0.15 nm/min.

A new IWO recipe was created, and the parameters were: Argon flow rate of 30 sccm, no 1%O<sub>2</sub> – 99%Ar flow, substrate temperature of 25 °C, chamber pressure of 3×10<sup>-3</sup> mbar, and power density of 0.62 W/cm<sup>2</sup>. The IWO deposition

rate changed as the power density varied.

### **Power density optimization**

The passivation degradation of the samples is reflected by the  $iV_{OC}$  difference before and after deposition. The properties of multiple  $n^+$  and  $p^+$  passivation samples were first measured by Sinton, followed by double-sided deposition of 75 nm IWO. In this experiment, the new recipe was applied, where the power remained at  $3 \times 10^{-3}$  mbar, but the power density varied in each deposition to: 1.23, 1.85, and 2.47 W/cm<sup>2</sup>. The sample properties were measured again after deposition.

### **Working pressure optimization**

Similar to the optimization power density step. The power density value for all IWO depositions at this point was 1.23 W/cm<sup>2</sup>. Other variables in the new recipe were kept steady and the total gas pressure was changed to: 1, 5, 9, 11, 20 ( $\times 10^{-3}$  mbar). After deposition the sample properties were measured again. There is one thing needed to mention that the SiO<sub>x</sub> formation method for passivation samples was NAOS in power density and working pressure optimization experimental, while it was changed to thermal oxidation in the following work.

### **Adding buffer layer to $p^+$ sample**

Different thicknesses of a-Si:H were deposited as buffer layers on  $p^+$  passivation samples by PECVD with the parameters shown in the Table 2.1. AZO (doping level =  $1 \times 10^{21}$  atoms/cc) was obtained by spatial ALD onto the  $p^+$  passivation samples (SiO<sub>x</sub> formation method was thermal oxidation). Since AZO is itself a TCO, however, the subsequent IWO thickness was 60 nm instead of 75 nm for the passivation sample.

- Recovery effect enhancement

### **Vacuum annealing temperature optimization**

After depositing the IWO, annealing treatment of the samples is required to obtain curing and optimize the IWO properties simultaneously. The samples was subjected in vacuum annealing by PECVD in Kavli (samples were processed with the optimized-IWO). And the annealing temperature effect on the passivation of the samples was investigated. Following the deposition of 75 nm optimized IWO on both sides of the symmetrical passivation samples, vacuum annealing was performed for 30 min at 300, 350, and 400 °C, respectively. Due to the temperature limitation of the equipment, the maximum temperature set was only up to 400 °C. The sample properties were characterized after completion of annealing.

- Solar cell fabrication

30 nm thick i/p stack and i/n stack were prepared on the front side and rear side of the poly – Si(O<sub>x</sub>) cell precursor, respectively. IWO films with nominal 75 nm and 150 nm thickness were sputtered on the front side and rear side with a hard mask, which defined five different cell regions on each wafer. Following sputtering, the cell precursors were annealed in vacuum at 400 °C for 30 minutes (optimized annealing recipe). Both front and rear metal contacts were preceded by screen printing: the used screen was designed with 70 μm line width, printing speed was 15 mm/s and no snap-off was applied. One should note that different surface texturing treatment were applied to the samples in order to reduce optical losses, the process is described in Section 2.4.1.

### 3.3. Sputtering damage reduction

#### 3.3.1. Power density optimization

The  $iV_{OC}$  reduction after IWO deposition was 34.6 mV and 16.9 mV for  $n^+$  and  $p^+$  samples (0.62 W/cm<sup>2</sup> in Figure 3.1). For minimizing the damage during IWO sputtering, the power density was tuned. As mentioned in Section 2.2, various particles generated during RF sputtering are the main reason for the passivation degradation of the sample. The energy carried by particles such as plasma is positively correlated with the sputtering power density, i.e., a larger power density results in a higher energy carried with the particles and a greater possibility of breaking the Si-Si bond or Si-H bond[51]. Therefore, it was observed in the Figure 3.1 that for  $n^+$  samples, the gap between  $iV_{OC}$  before and after IWO deposition increased as the power density continued to grow larger as the power density is above 1.23 W/cm<sup>2</sup>. However, the power density also influences the deposition rate. A small deposition power density implies a longer time required for the sample to deposit 75 nm IWO, resulting in a prolonged exposure to energetic particles, light, and heat as well, which is unfavorable for passivation as well. Therefore, when the power density was 0.62 W/cm<sup>2</sup>, the drop in  $iV_{OC}$  was instead greater than 1.23 W/cm<sup>2</sup>. With the see-saw of particle energy versus deposition time, the sample at 1.23 W/cm<sup>2</sup> exhibited the smallest drop in  $iV_{OC}$ , which was 6.3 mV. For the  $p^+$  samples,  $iV_{OC}$  all showed a decrease of about 10 mV when the deposition power was greater than 1.23 W/cm<sup>2</sup>. Collectively, 1.23 W/cm<sup>2</sup> has been regarded as the optimal deposition power density for IWO, and the deposition rate was 0.051 nm/s. The relationship between lifetime and minority carrier density (MCD) of  $n^+$  sample deposited with IWO at 1.23 W/cm<sup>2</sup> was also explored as shown in Figure 3.2. Comparing the curves before and after IWO deposition, a noticeable decrease can be found at an injection level of  $1 \times 10^{15}$  cm<sup>-3</sup>. And when the minority carrier concentration was raised to  $5 \times 10^{15}$  cm<sup>-3</sup>, a gap was observed as well, but narrower than the one at  $1 \times 10^{15}$  cm<sup>-3</sup>. This suggests that SRH recombination and Auger

recombination were responsible for the passivation degradation after IWO deposition, in particular SRH recombination. We speculate that this is because high-energy particle bombardment during IWO sputtering broke Si-Si or Si-H bonds on the Si surface, increasing surface defects (e.g., hanging bonds), which greatly enhanced defect-assisted SRH recombination[16].

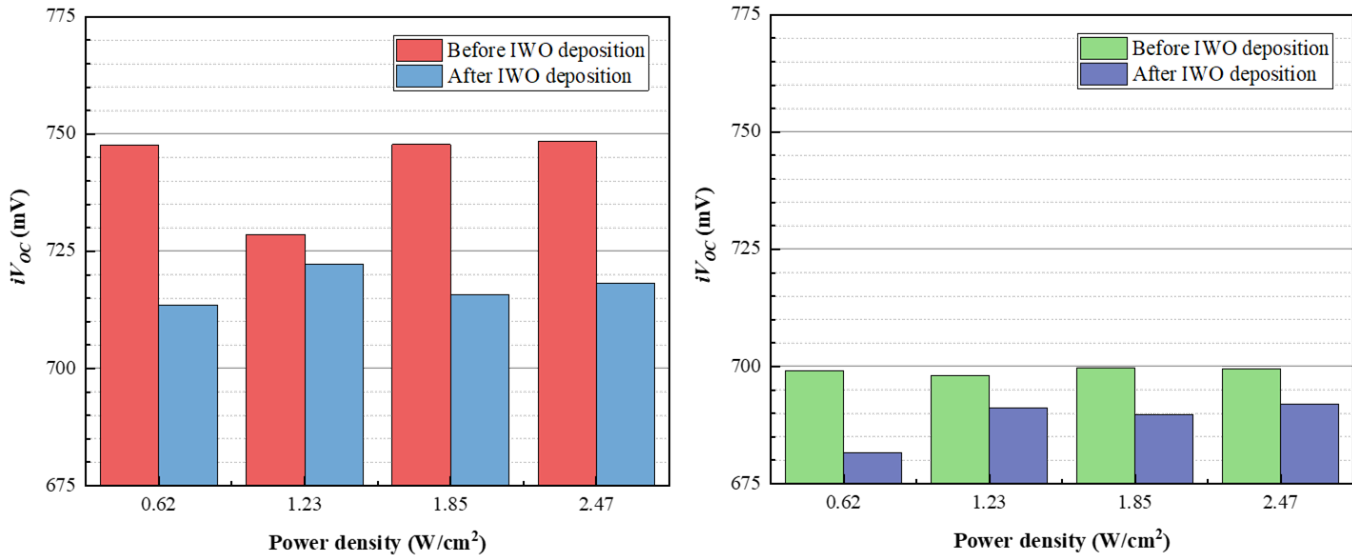


**Figure 3.1:** The  $iV_{OC}$  of  $n^+$  (left) and  $p^+$  (right) passivation samples before/after 75nm IWO deposition with various sputtering power density (working pressure =  $3 \times 10^{-3}$  mbar).

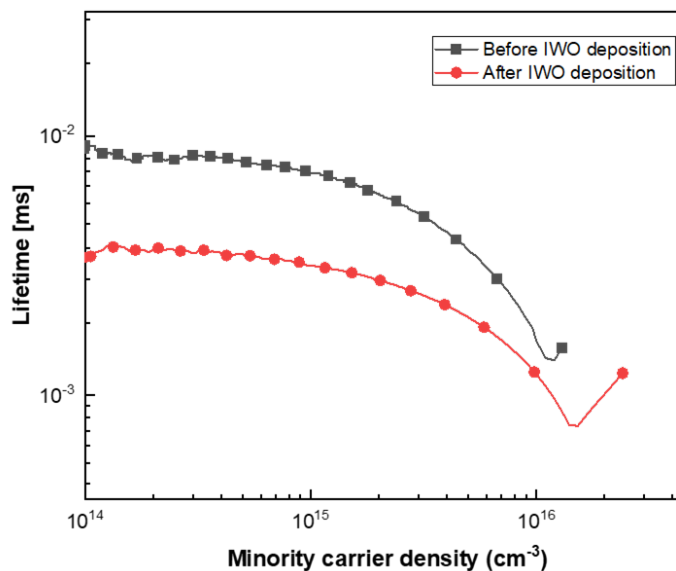


**Figure 3.2:** The lifetime as a function of minority carrier density for a  $n^+$  passivation sample before/after 75nm IWO deposition (power density =  $1.23 \text{ W}/\text{cm}^2$ , working pressure =  $3 \times 10^{-3}$  mbar).

### 3.3.2. Working pressure optimization

The comparison of  $iV_{OC}$  of  $n^+$  and  $p^+$  samples after IWO deposition at different working pressures is presented in Figure 3.3. At an working pressure of  $5 \times 10^{-3}$  mbar, the  $n^+$  sample  $iV_{OC}$  showed the smallest decline value, 4.7 mV. Similar to the power density, this optimal value is also determined by a combination of factors. The possibility of plasma collisions with surrounding gas particles is enhanced with higher working pressure, which consumes the energy of the plasma[16]. As a result, bond breakage on the silicon surface due to high-energy particle bombardment can be prevented to a large extent, protecting the existing passivation. Nevertheless, this also leads to a slower deposition rate and a longer time for the formation of the initial protective layer on the silicon surface, which in turn aggravates the passivation degradation[52]. As for the  $p^+$  samples, when the pressure was less than or equal to  $5 \times 10^{-3}$  mbar, the drop of the sample  $iV_{OC}$  was 7.9 mV, indicating an insensitivity to pressure changes at this time. But as the pressure increased to  $13 \times 10^{-3}$  mbar, the decline in  $iV_{OC}$  was more than 10 mV. Comprehensively,  $5 \times 10^{-3}$  mbar was regarded as a preferable selection.

Summarily, the parameters for the optimized IWO recipe were determined: argon flow rate of 30 sccm, no  $1\%O_2 - 99\%Ar$  flow, substrate temperature of  $25^\circ C$ , chamber pressure of  $5 \times 10^{-3}$  mbar, and power density of  $1.23 W/cm^2$ . The IWO deposition rate was  $0.05 nm/s$ . We call this optimized IWO recipe as optimized-IWO in following work. And the  $SiO_x$  formation method in following experiments was changed to thermal oxidation process for better passivation quality[53].

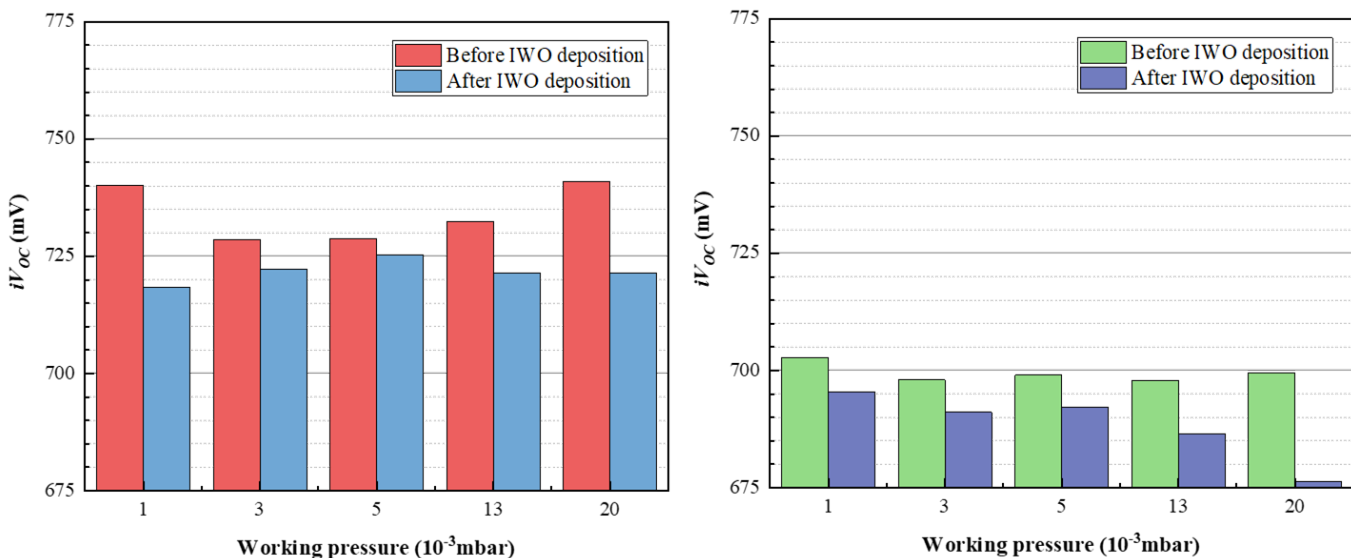


**Figure 3.3:** The  $iV_{OC}$  of  $n^+$  (left) and  $p^+$  (right) passivation samples before/after 75 nm IWO deposition with various sputtering working pressure (power density =  $1.23 W/cm^2$ ).

### 3.3.3. Buffer layer for $p^+$ sample

From Figure 3.3, the  $p^+$  sample was more susceptible to sputtering damage compared to the  $n^+$  sample, leading to a greater reduction in the sample  $iV_{OC}$ . For this reason, hydrogenated boron-doped amorphous silicon (a-Si:H) of different thicknesses was deposited on the sample surface as a buffer layer whose structure is illustrated in Figure 3.4. Figure 3.5 demonstrates the changes of  $iV_{OC}$  after 75 nm optimized IWO deposition, as the thickness of pre-deposited a-Si:H varied. The insertion of only 2 nm a-Si:H between IWO and poly – SiO<sub>x</sub> was able to effectively reduce the loss of  $iV_{OC}$  as well (from 7 mV to 5 mV). This might be attributed to SRH recombination suppressed since a-Si:H served as a physical barrier against high-energy particle bombardment and avoided the formation of excessive defect. Moreover, there was something else: at a thickness of 5 nm, the  $iV_{OC}$  after depositing 75 nm IWO was even higher than the initial value. This might be credited to that the thicker a-Si:H significantly absorbed the UV illumination, which was also harmful for the passivation. The physical protection coupled with the UV illumination absorption resulted in an increase in  $iV_{OC}$  of 6 mV after IWO deposition for a sample with 20 nm a-Si:H inserted. However, it is not practical to add an excessively thick a-Si:H for a solar cell, since parasitic absorption of a-Si:H is severe. Hence, 8 nm was selected as the thickness of the buffer layer for subsequent experiments.

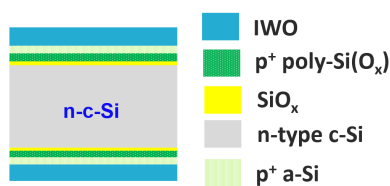


Figure 3.4: The structure for  $p^+$  passivation sample with a-Si:H as buffer layer.

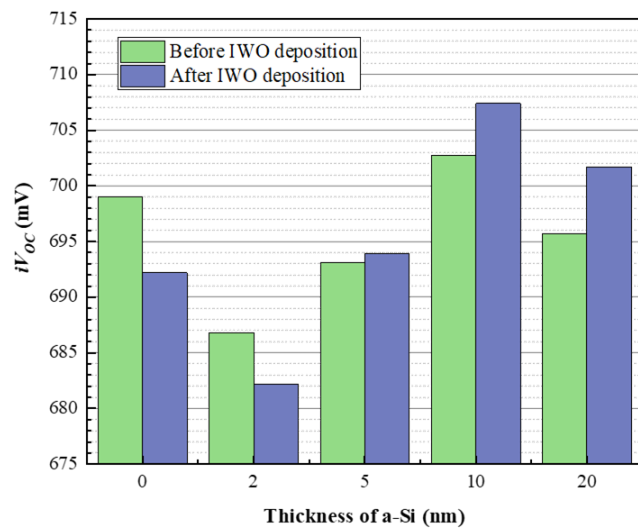


Figure 3.5: The  $iV_{OC}$  of  $p^+$  passivation samples applied various thickness a-Si:H before/after 75nm IWO deposition.

### 3.4. Recovery effect enhancement

#### 3.4.1. Annealing temperature optimization

The annealing can effectively restore the passivation degradation due to the formation of Si dangling bonds[16]. And the temperature has a significant effect on the effect of passivation recovery. For the  $n^+$  sample, as illustrated in the Figure 3.6, after 30 minutes of high-temperature vacuum annealing, the  $iV_{OC}$  showed a remarkable improvement compared with IWO as-deposited, and the higher the temperature, the greater the enhancement. When the temperature reached 400 °C, the  $iV_{OC}$  was boosted by 49 mV to 748.8 mV, even 15 mV higher than the initial value. Figure 3.7 demonstrates the lifetime-MCD curves of the  $n^+$  sample after IWO deposition versus after annealing at 400 °C. Regardless of the high or low injection levels, the lifetimes were greatly promoted after the samples underwent annealing, implying that both SRH recombination and Auger recombination were effectively suppressed. The  $p^+$  samples exhibited the same trend as the  $n^+$  samples: higher annealing temperatures resulted in better passivation recovery. When the annealing temperature was 400 °C, the  $iV_{OC}$  increased by nearly 60 mV. In summary, a vacuum annealing temperature of 400 °C is the most preferred.

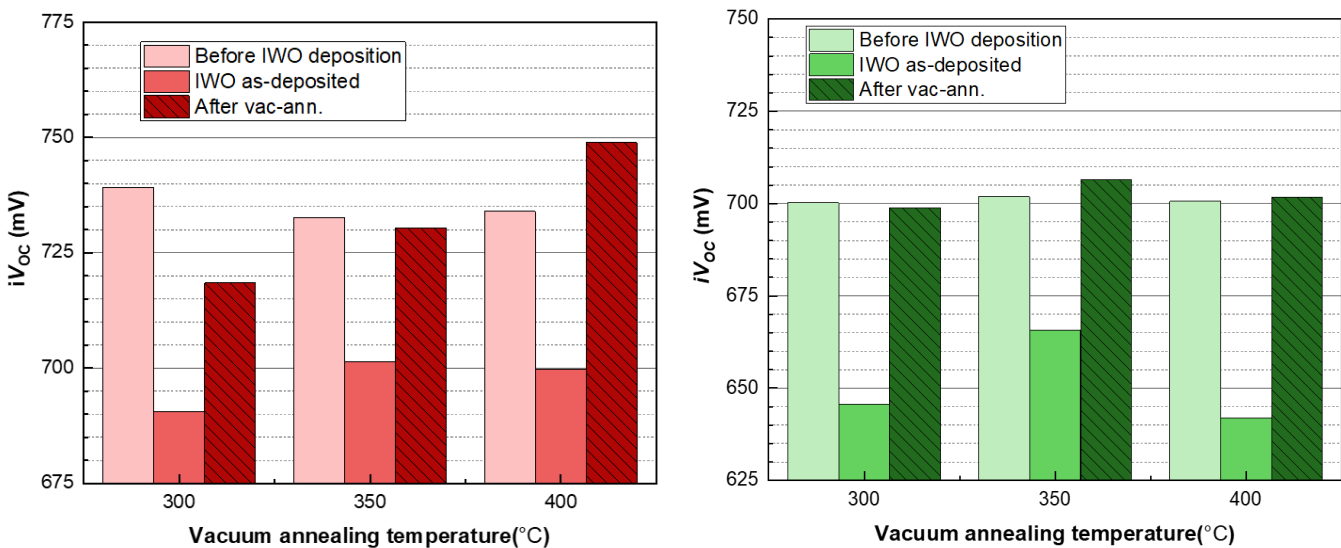


Figure 3.6: The  $iV_{OC}$  of  $n^+$  (left) and  $p^+$  (right) passivation samples after IWO deposition and 30 – min vacuum annealing under various temperature.

### 3.5. IWO properties

The properties of the optimized IWO before and after annealing are listed in the Table 3.1. After annealing, the properties of IWO were greatly improved:  $N_e$  dropped, reducing free carrier absorption;  $\mu_e$  raised, enhancing carrier transport capability

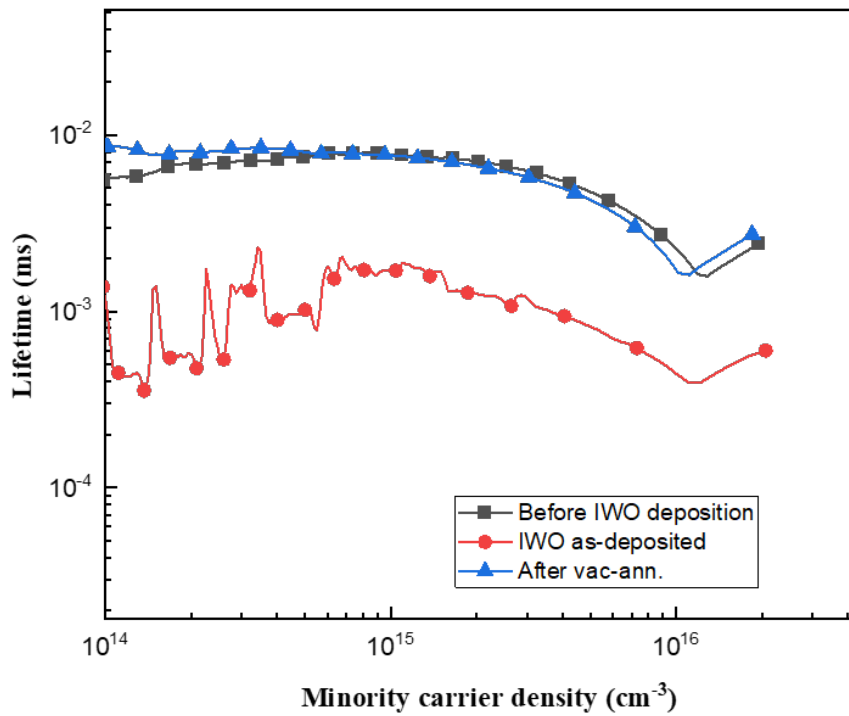


Figure 3.7: The lifetime as a function of minority carrier density for a  $n^+$  passivation sample after IWO deposition and 400 °C vacuum annealing for 30 mins.

and ensuring conductivity. When the annealing temperature was greater than the crystallization temperature (180 °C), the film transformed from the amorphous phase to the crystalline phase, favorable for oxygen movement. As a result, the oxygen vacancy density declined,  $N_e$  decreased, and  $\mu_e$  increased after annealing[54].

Table 3.1: The properties of optimized IWO.

IWO	$N_e$ ( $\text{cm}^{-3}$ )	$\mu_e$ ( $\text{cm}^2/\text{Vs}$ )	$\rho$ ( $\Omega \text{ cm}$ )
As-deposited	$2.98 \times 10^{20}$	14	$1.50 \times 10^{-3}$
400 °C vac-ann. for 30min	$2.41 \times 10^{20}$	48	$5.41 \times 10^{-4}$

### 3.6. Cell performance

Based on the previous results, batches of solar cells with different treatments were prepared and the basic structure is shown in Figure 3.8. The values mentioned subsequently are the average of 5 cells in each batch. In order to simplify the expression, the batch of cells is directly represented by cell in the following. The results are divided into three groups for control analysis.

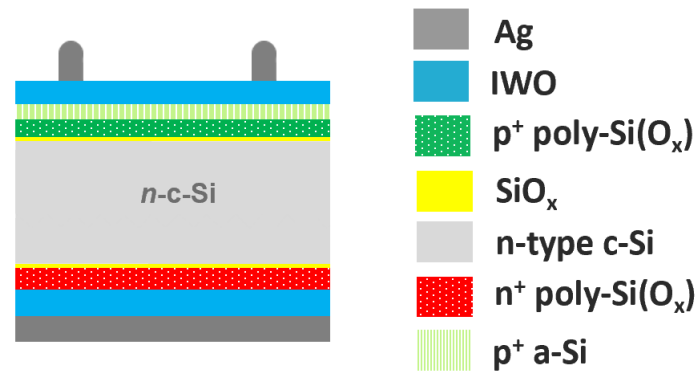


Figure 3.8: The first basic structure for poly – Si(O<sub>x</sub>) cell applied 8 nm a-Si:H as buffer.

### 3.6.1. 8 nm a-Si:H as buffer layer

The variable in the first group is the application with or without a buffer layer (Figure 3.9). Both cells in this group were double-sided polished (DSP) and deposited with ref-IWO. The only difference between them was the second cell used 8 nm a-Si:H as a buffer layer, while the first cell did not have any buffer layer.

Comparing the two cells, the  $V_{OC}$  of the second cell was 13.8 mV higher than that of the first cell, which suggested that a-Si:H did protect the cell precursor to some extent and reduced the sputtering damage generated during IWO deposition, consistent with the results in Section 3.3.3. However, the presence of a-Si:H induced parasitic absorption, as indicated by the decrease in  $J_{SC}$  at 1.6 mA/cm<sup>2</sup>. Moreover, the fill factor dropped substantially (5.2%) after the adoption of a-Si:H, corresponding to the large increase in contact resistivity shown in right picture of Figure 3.9. This may be related to the relatively poor conductivity of a-Si:H and the formation of interfacial oxides. Ultimately, the cell with a-Si:H as the buffer layer showed a 1.5% efficiency drop compared to the cell without any buffer layer. This result implies that hydrogenated amorphous silicon was not ideal as a buffer layer here.

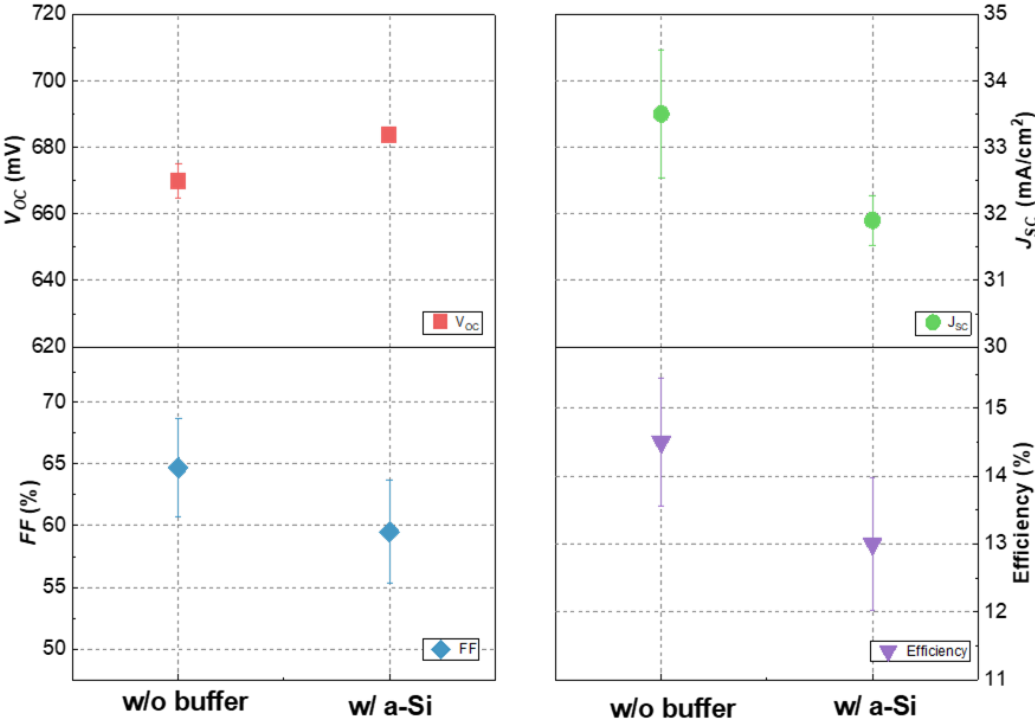


Figure 3.9: The performance of poly-Si(O<sub>x</sub>) cells with/without a-Si:H as buffer layer. The values shown are the average based on 5 cells from the same batch.

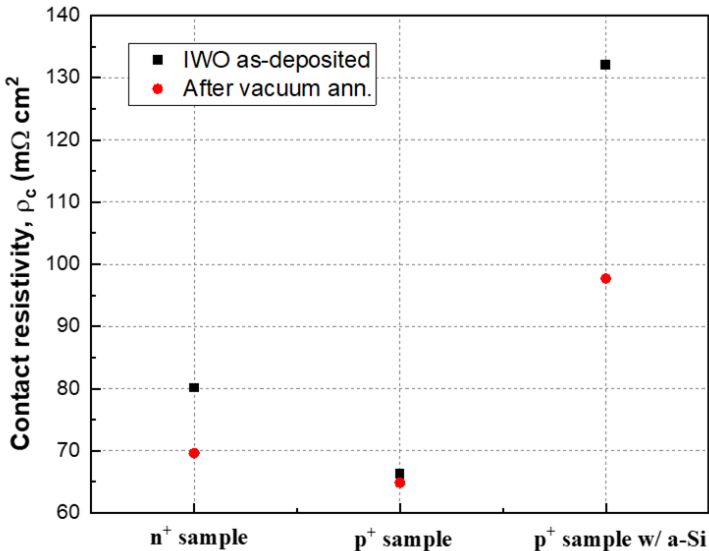
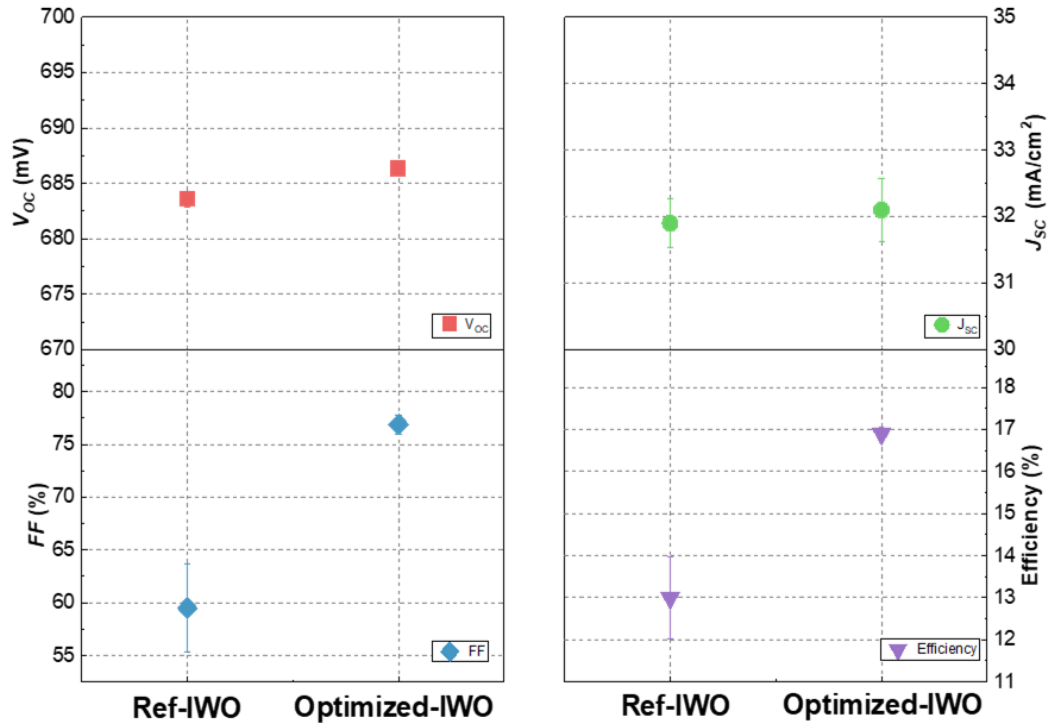


Figure 3.10: The contact resistivity for different samples.

### 3.6.2. IWO optimization

The cells in this group (left one in Figure 3.11) were still polished on both sides and applied a-Si:H as a buffer, but the second cell employed the optimized IWO ( $1.23 \text{ W/cm}^2$ ,  $5 \times 10^{-5} \text{ mbar}$ ). This IWO optimization brought a significant improvement in  $FF$ , from 59% to 76%. As a result, the efficiency jumped from 13.0% to about 16.9%. Thus, it can be said that the optimized IWO recipe shows a better electrical performance than the reference IWO and the deposition speed is faster.



**Figure 3.11:** The performance of poly-Si(O<sub>x</sub>) cells: with different IWO deposition. The values shown are the average based on 5 cells from the same batch.

### 3.6.3. The texturing treatment

The variable of the third group is the texturing: the first cell is double-sided polished (DSP), while the second cell is single-sided textured (SST) and the last one is double-sided textured (DDT). All three cells deposited 8 nm a-Si:H as a buffer layer and used optimized IWO recipe. From the Figure 3.12, it is known that texturing influenced  $V_{OC}$  and  $J_{SC}$  greatly. The texturization was detrimental to  $V_{OC}$  and indeed helped the optical performance of the cells. The second cell (SST) achieved the highest efficiency of all cells with 17.4%.

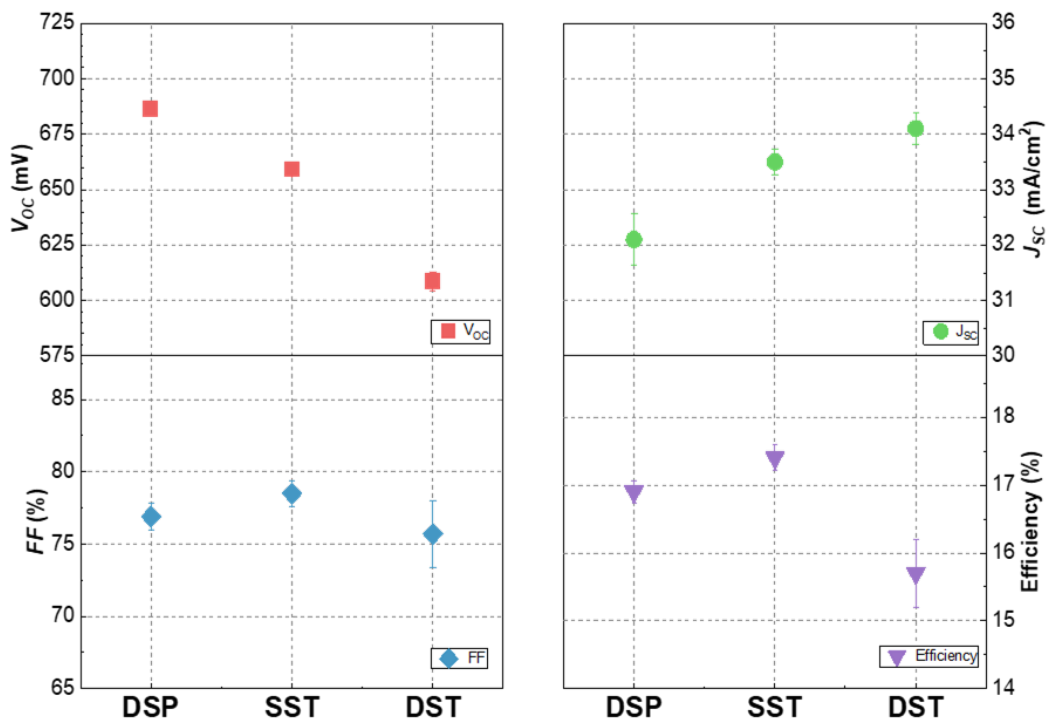


Figure 3.12: The performance of poly-Si(O<sub>x</sub>) cells with different texturing treatment. The values shown are the average based on 5 cells from the same batch.

### 3.7. Other improvement

#### 3.7.1. AZO as buffer

Due to the poor performance of hydrogenated amorphous silicon (as described in Section 3.6.1), 20 nm AZO prepared by ALD was tried as a buffer layer. From the Figure 3.13, it can be found that the  $iV_{OC}$  did not decrease much after depositing 20 nm AZO; after depositing 60 nm IWO, the  $iV_{OC}$  declined by 5 mV; moreover, the  $iV_{OC}$  improved to 690 mV after 30 min vacuum annealing at 400 °C, which was 3 mV lower than initial value. This result seems to be not as effective as the protection brought by a-Si:H. However, when we compare their minority lifetime, it becomes clear that the sample with 20 nm AZO deposited can recover to the initial 70% level after vacuum annealing, compared to 43% for the sample with a-Si:H. This enhancement can be attributed to the following reasons: first, the ALD itself was damage-free, which did not introduce additional sputtering damage, therefore the sample did not show a noticeable decrease in lifetime and  $iV_{OC}$  after deposition of 20 nm AZO. Then, the deposited AZO was hydrogenated, which provided extra hydrogen to the sample and enhanced the passivation effect. Finally, since the band gap of AZO is larger than that

of a-Si:H, the thickness of AZO can be increased to 20 nm to enhance the protection effect without worrying about its excessive parasitic absorption.

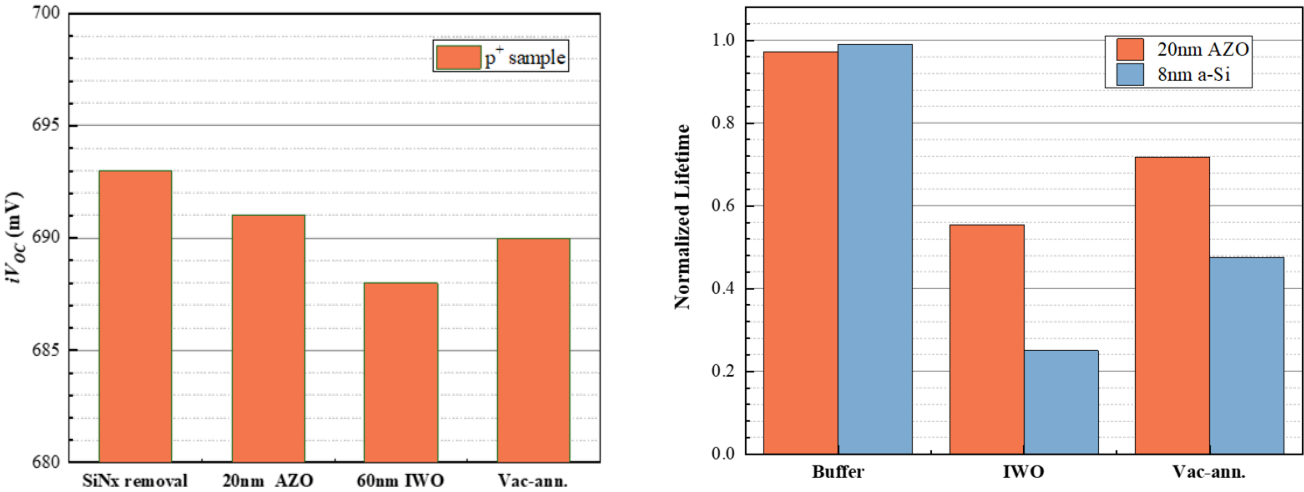


Figure 3.13: Left: the  $iV_{oc}$  of  $p^+$  passivation samples after 20 nm ALD AZO, 60 nm IWO deposition and vacuum annealing  
Right: the normalized lifetime of  $p^+$  passivation samples after deposition of buffer layer (a-Si:H or AZO) & IWO and vacuum annealing.

# 4

## Screen printing optimization

### 4.1. Introduction

Metallization is necessary for solar cells to improve conductivity and collect electrons. The quality of metallization can greatly affect the efficiency of solar cells, so it is crucial to find the optimal metallization conditions.

In this section, we focus on the optimization of fine grids. By modifying the parameters involved in screen printing, a grid with excellent continuity, small width and large height is printed. The line resistance, morphology, and cross-section of the grid lines are characterized. Meanwhile, based on the optimized setup, we provide a new screen printing workflow for subsequent laboratory screen printing users.

### 4.2. Experimental

- Materials

All samples were 280  $\mu\text{m}$  silicon wafers with texturing treatment. The silver paste used was purchased from Kyoto Elex, with product serial number DD-1760Q-116. The used organic solvent was Butyldiglycol acetate.

- Initial screen printing

In our laboratory, the silver paste is normally taken out of the freezer in advance and left for at least 3 hours to warm up to room temperature. No further treatment of the silver paste is done. The screen employed is typically with a mesh number of 380 and a grid width of 70 microns. During the printing process, instead of snap-off, on contact printing is performed. The squeegee speed is 15 mm/s. Drying and curing are carried out in an oven at 170  $^{\circ}\text{C}$  for 1 min and 30 min respectively. The grid obtained under the above conditions was used as the baseline and compared with the optimized grids.

- Characterization

The grid morphology was obtained by optical microscopy (Microscope Olympus in EKL100) with a magnification of 5x. The cross-sectional images were collected by a scanning electron microscope (Hitachi Regulus 8230 in EKL100) at 1500x magnification. The grid line resistance was measured in ohm mode of the multimeter. And the viscosity of silver paste was measured by the viscometer in ESP basement.

### 4.3. Initial screen printing setup

Figure 4.1 shows the shape of the grid lines as obtained with the initial screen printing setup in our lab. It is apparent from the figure that the grid had a good continuity and a relatively three-dimensional shape. However, an obvious spreading of the paste occurred, with a width of  $155.3 \mu\text{m}$ , exceeding by far the set width of  $70 \mu\text{m}$ . This widening will undoubtedly cause additional shading loss, resulting in deterioration of the cell performance.

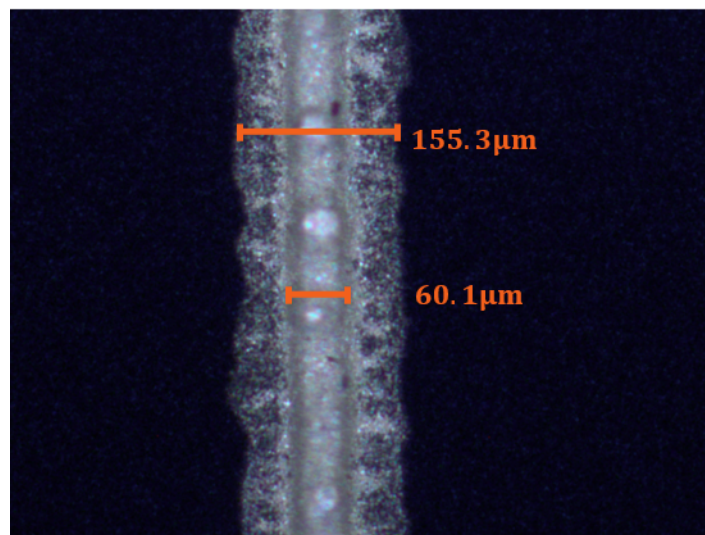


Figure 4.1: The morphology of grid printed under lab conventional screen printing condition.

Considering the spread width of the silver paste after printing of the screen with  $70 \mu\text{m}$  opening, we decided to change the screen printed stencil: use  $40 \mu\text{m}$  opening width. However, the narrowed opening width also made printing more difficult, as shown. The resulting grid showed multiple breaks, poor continuity, and nearly two-dimensional shapes, leading to a sharp drop in fill factor ( $FF$ ).

### 4.4. Optimized screen printing

In order to obtain fine grids with good continuity and high aspect ratio, several parameters involved in screen printing were optimized, including the pretreatment of the paste (adding organic solvents) and the optimization of printing settings

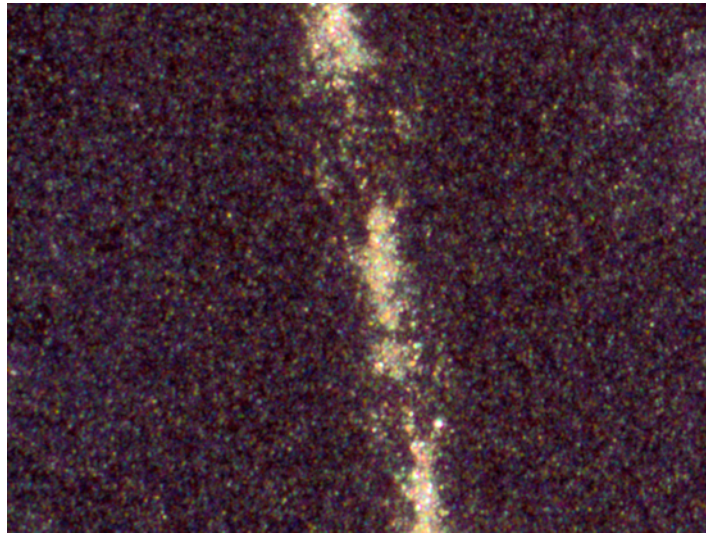


Figure 4.2: The morphology of grid printed with 40  $\mu\text{m}$  opening.

(adjustment of snap-off distance and squeegee speed).

#### 4.4.1. Viscosity of paste

The viscosity of the initial paste without any added solvent was 375 Pa·s (viscometer rotating at 10 rpm). The excessively high viscosity made it difficult for the silver paste to pass through the narrow openings, resulting in poor continuity of the grid. In an attempt to reduce the viscosity of the silver paste, a specific organic solvent was added to it. The Figure 4.3 displays the variation of the viscosity of the silver paste with the weight fraction of the added organic solvent: the more organic solvent is added, the less viscous the silver paste becomes, and the variation is essentially linear. Figure 4.4 shows the grid lines printed for pastes with different weight fractions of added organic solvents, while leaving other conditions unchanged. As the solvent mass fraction raised from 0 to 0.37%, the mass of paste reaching the wafer through the opening increased significantly and a near-square cross section was obtained at 0.37%, ensuring a low series resistance. But by continuing to increase the amount of organic solvent added, the viscosity dropped below 250 Pa·s and the grid aspect ratio reduced until it collapsed (e.g., 0.74%). Based on the cross-sectional shape of the grid, 0.37% was considered as the preferred organic solvent weight fraction. However, although the continuity of the grid was improved with the 0.37% organic solvent added silver paste, as shown in the Figure 4.5, there were still grid breaking (e.g. at the connection with the main grid). Therefore, the continuity still needs to be further enhanced to ensure no breakage.

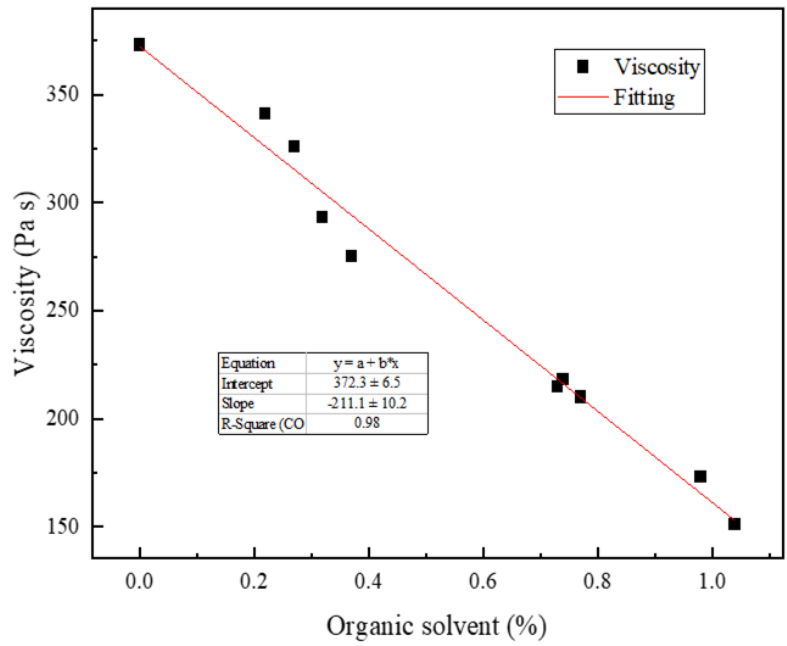


Figure 4.3: The viscosity of silver paste as a function of adding organic solvent (weight fraction).

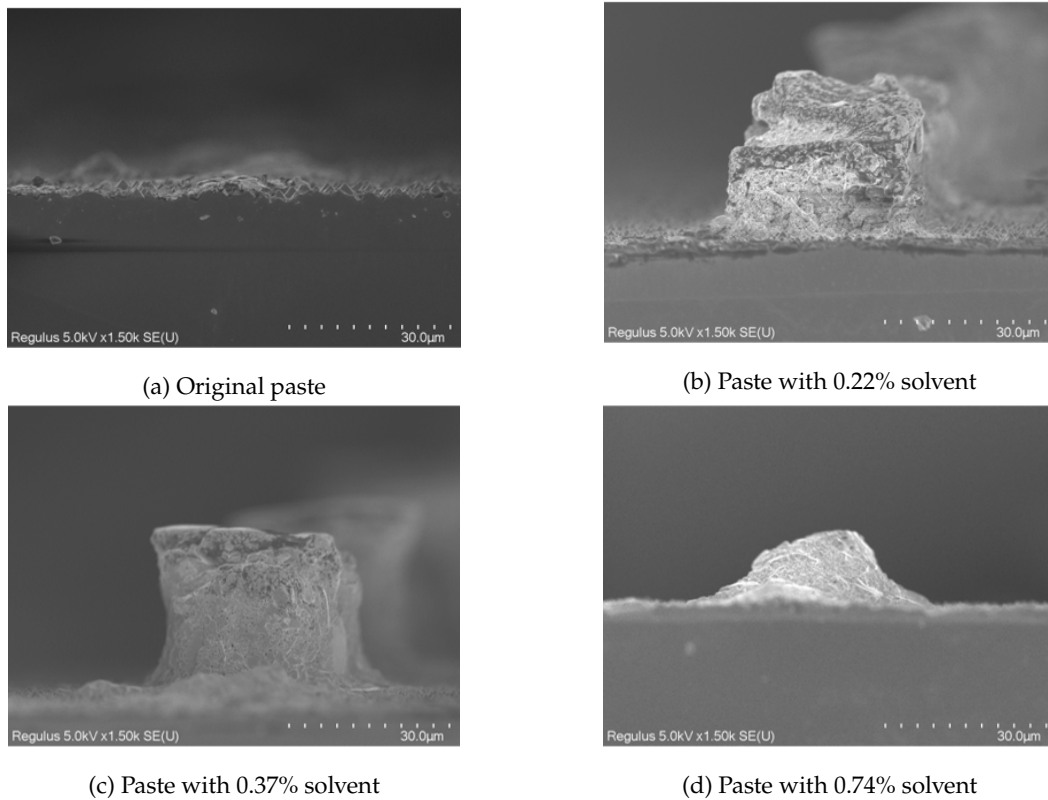
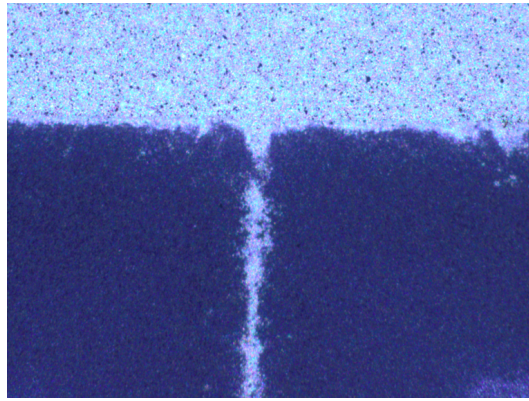


Figure 4.4: The SEM images for the cross-section of the grids with different weight fraction of organic solvent.



**Figure 4.5:** The image observed by optical microscopy for the grid with 0.37% weight fraction of organic solvent.

#### 4.4.2. Snap-off distance

To allow more paste to pass smoothly through the opening in the screen plate, snap-off was used instead of the initial contact printing. Figure 4.6 indicates the variations in the continuity when the snap-off distance was changed. This improvement can be attributed to the presence of snap-off, providing a difference in air pressure between the top and bottom surfaces of the screen[55]. This pressure difference promoted the paste to dislodge from the screen and completes a heavier deposition. But this unsealed printing also caused the silver paste to spread: when the snap-off distance was 0.02 mm, the silver paste underneath the grid spread to  $76.5 \mu\text{m}$ , and for the distances of 0.12 mm and 0.22 mm, this widening was  $101.5 \mu\text{m}$  and  $120.8 \mu\text{m}$ , respectively. In a comprehensive view, one can enhance the continuity of the grid by setting the snap-off distance to 0.02 mm in place of the conventional on-contact printing. But it is necessary to reduce the extension of the silver paste in the next optimization step to avoid the additional optical loss.

#### 4.4.3. Squeegee speed

A further parameter to be tuned was the speed of the squeegee. Generally, the silver paste through the opening will regain its solidity as soon as the squeegee leaves. Thereby, the faster the squeegee progresses, the quicker the silver paste solidifies and the fewer the spread. The paste spreading width for seven separate sets of grid printed at different velocities is shown in Figure 4.7, where 15 mm/s was the initial value. The initial spreading width was  $76.5 \mu\text{m}$ . When the squeegee moving rate increased, the paste widening decreased remarkably, and particularly at 30 mm/s, the spreading width was below  $60 \mu\text{m}$ . As can be seen from the image (Figure 4.8), however, when the speed was increased to 35 mm/s, the grid lines showed incomplete printing, which was primarily due to the short printing time caused by the excessive speed. Figure 4.9 shows the cross section of the optimized grid line. The width was  $36.3 \mu\text{m}$  and the height was  $24.9 \mu\text{m}$ . Even though the aspect ratio cannot be calculated precisely due

to the silver paste spreading close to  $60 \mu\text{m}$  at the bottom, its continuity and shape satisfied the requirements.

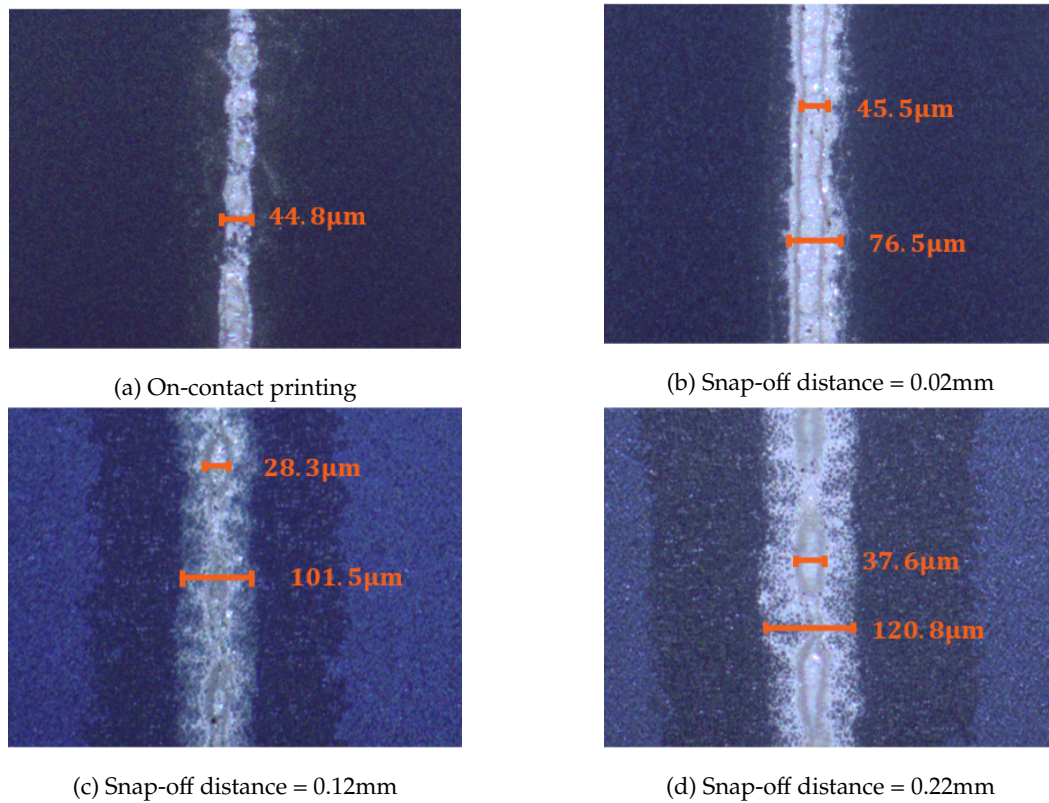


Figure 4.6: The shape of the printed grids at different snap-off distances.

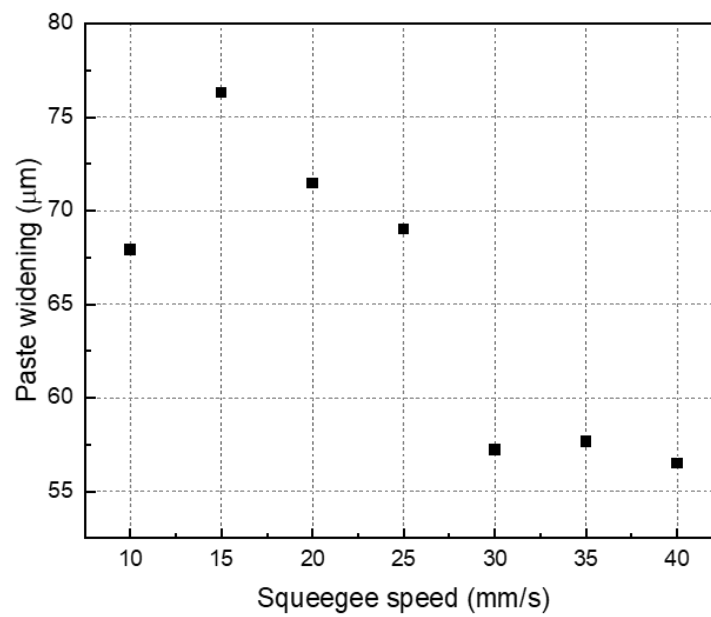


Figure 4.7: The paste spreading width for seven separate sets of grid printed at different velocities.

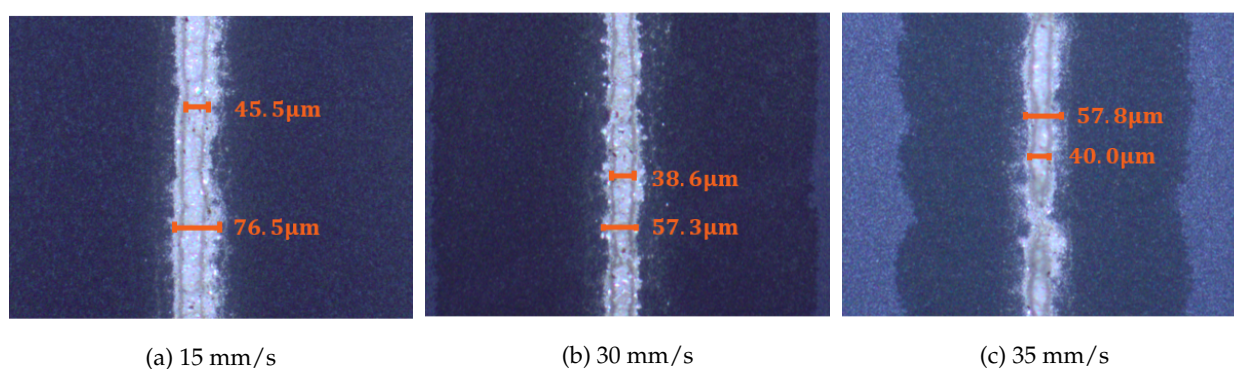


Figure 4.8: The shape of the printed grids at different squeegee speed.

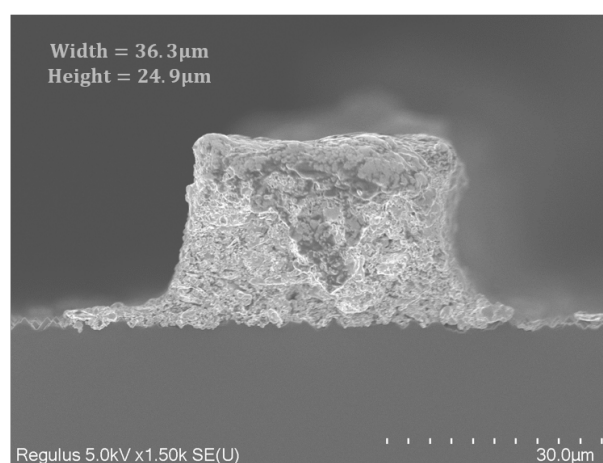


Figure 4.9: The SEM image for the cross-section of the grid with 30 mm/s squeegee speed.

## 4.5. Flowchart

A new flowchart for screen printing can be concluded on the basis of the above optimization, shown as Figure 4.10. The first step is to add organic solvent to the silver paste from the freezer with a weight fraction of 0.37%. It is normally done in the fume hood of the sample preparation room in the ESP lab basement. Mixing is indispensable after the addition of solvent. The centrifuge speed is set to 500 rpm and the duration is proportional to the mass of the paste: at a minimum of 3 minutes for every 40 gram paste ( tested to ensure that the paste is well stirred and the temperature is raised to 25 °C). The viscosity of the paste after agitation is an essential reference which should be in the range of 280-300 Pa·s at a viscometer speed of 10 rpm. Once the pre-treatment of the paste is completed, the experimental operation is switched to a dedicated screen printing room in the ESP basement. A screen with a mesh number of 380 and a linewidth of 40 μm should be selected and installed to the screen printer. In the recipe setting, the snap-off distance should be set to 0.02 mm ( NOTE, the instrument setting of printer in ESP requires an extra 1.5 mm initial value, and the wafer thickness, i.e., the setting should be the sum of the three, 1.8 mm), while

the squeegee speed should be changed to 30 mm/s. After each printing, the sample has to be dried in a 150 °C oven for 10 minutes; after both sides are finished printing, the sample should be placed in a 200 °C oven for 40 minutes, to create an effective contact between the metal and the cell precursor. At this stage, the screen printing is accomplished.

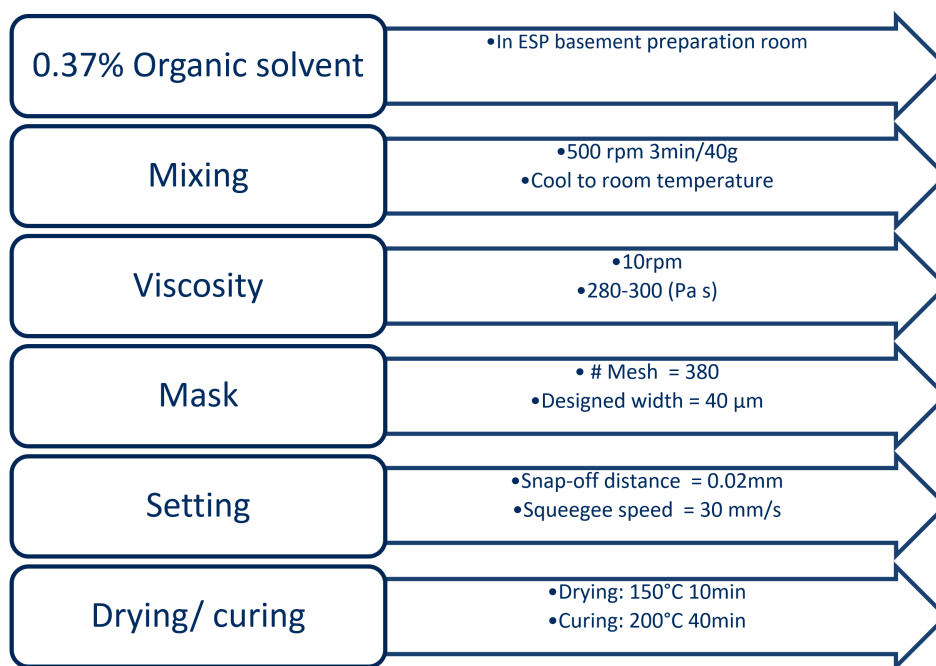


Figure 4.10: The flowchart for optimized screen printing.

# 5

## Cell fabrication

### 5.1. Introduction

In Chapter 3, different methods are employed to reduce the passivation degradation caused by the IWO deposition process. The power density and pressure in the IWO deposition recipe were adjusted and the post-annealing temperature was optimized. Meanwhile, a-Si:H was inserted as a buffer layer between  $p^+$  poly – Si(O<sub>x</sub>) and IWO to mitigate the sputtering damage. On this basis, the first cells were prepared with a  $p^+$  poly – Si(O<sub>x</sub>) front surface. cell data showed that the optimized IWO formulation had superior electrical properties compared to the reference IWO, resulting in a substantial increase in  $FF$ . Although a-Si:H as a buffer layer could enhance the  $V_{OC}$  of the cell to some extent, it would lead to additional parasitic absorption. Furthermore, the single-sided textured treatment has better overall performance compared to the double-sided polished or double-sided textured. Among all the fabricated cells, one with optimized IWO, 8 nm a-Si:H, and single-sided textured treatment exhibited the highest efficiency of 17.4%.

In Chapter 4, optimization of the laboratory's existing screen printing was carried out. The commonly used 70  $\mu\text{m}$  line width screen was replaced by a 40  $\mu\text{m}$  screen with the aim of reducing the shadow loss caused by the metal electrodes. Simultaneously, printing with snap-off was used to improve the continuity of the grid. The influence of squeegee speed on the width of the silver paste widening was further investigated, revealing that the widening width could be controlled within 60  $\mu\text{m}$  at 30 mm/s. Under these conditions, the printed grid lines shown a three-dimensional shape and good continuity, and the width of the silver paste widening was relatively narrow.

Combined with the above experimental results, the poly – Si(O<sub>x</sub>) cells was fabricated. As a reference from the performance of the first batch of cells, this batch was made with optimized IWO, and the front side was textured rather than polished. But,

$n^+$  poly – Si(O<sub>x</sub>) was placed on the front side to reduce the passivation loss caused by the textured p+ surface during the cell precursor preparation, and simultaneously to suppress the possible parasitic absorption by the buffer layer.

## 5.2. Experimental

- Cell precursor

The basic structure of this batch of cells is shown in the Figure 5.1. All cells were textured on the front side and polished on the rear side. The  $n^+$  poly – Si(O<sub>x</sub>) contact structure was placed on the front side. The specific steps for the cell fabrication are shown in Section 2.4.1.

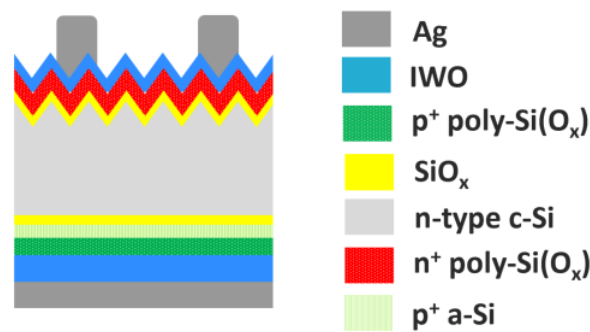


Figure 5.1: The structure for poly – Si(O<sub>x</sub>) cell, with  $n^+$  poly – Si(O<sub>x</sub>) on the front side.

- Buffer layer

Two types of buffer layer were used here: 8 nm a-Si:H and 20 nm AZO. The processing parameters are same as described in Section 3.2.

- IWO deposition and post-annealing

The ultimate IWO recipe (with O<sub>2</sub>) was not applied due to the equipment problem. The specific parameters for used IWO recipe are set as follows: Argon flow rate of 30 sccm, no 1%O<sub>2</sub> – 99%Ar flow, substrate temperature of 25 °C, chamber pressure of  $5 \times 10^{-3}$  mbar, and power density of 1.23 W/cm<sup>2</sup>. The yielded deposition rate is 0.55 nm/s. The annealing used was a vacuum anneal at 400 °C for 30 minutes.

- Metallization

The metallization used was screen printing, as always. As a comparison variable, however, the screen printing before and after optimization was employed separately. The specific steps of the pre-optimized screen printing (later referred to as ref-SP) are described in Section 4.2, while the post-optimized screen printing (later referred to as optimized-SP) is shown in Section 4.5. Optimization steps

mainly include: adding organic solvent with a weight fraction of 0.37%, selecting a screen with a line width of 40  $\mu\text{m}$ , setting the snap-off distance to 0.02 mm, changing the squeegee speed to 30 mm/s, adjusting the drying conditions to 150  $^{\circ}\text{C}$  for 10 min, and curing conditions to 200  $^{\circ}\text{C}$  for 40 min.

### 5.3. Cell performance

#### 5.3.1. Screen printing optimization

The variable for the first group of cells is screen printing. Both batches of cells did not apply any buffer layer, the only difference was that the first batch of cell used reference screen printing (ref-SP) while the second batch of cell used optimized screen printing (optimized-SP). The average values of cell parameters for each batch are listed in the Table 5.1. Comparing the average parameters, the optimized-SP batch had a higher  $J_{\text{SC}}$  of 2.0  $\text{mA}/\text{cm}^2$  compared to ref-SP. This improvement was expected since the optimized-SP samples had thinner grids and a much narrower extended width of silver paste than ref-SP (57.3  $\mu\text{m}/155.3 \mu\text{m}$ ). The smaller electrode shading area enabled the cell to absorb more light. And the enhancement of  $FF$  could be attributed to the curing at 200  $^{\circ}\text{C}$  for 40 minutes which allowed the metal electrodes to form a closer contact with the cell. Meanwhile the cell grids were relatively thick, making the series resistance low. The final average efficiency of the optimized-SP samples was improved by 2.4% to 18.5%. And the best optimized-SP cell achieved the champion efficiency (18.9%) in this thesis, and  $J - V$  curve and parameters' values are shown in Figure 5.2.

**Table 5.1:** The average parameters for the cells applied ref-SP and optimized-SP. The cell area is 4.0  $\text{cm}^2$ .

Cell	$J_{\text{sc}}$ ( $\text{mA}/\text{cm}^2$ )	$V_{\text{oc}}$ (mV)	$FF$ (%)	Efficiency, $\eta$ (%)
Ref-SP	$36.3 \pm 0.8$	$671.0 \pm 3.1$	$65.9 \pm 1.2$	$16.1 \pm 0.1$
Optimized-SP	$38.3 \pm 1.5$	$673.0 \pm 0.8$	$71.9 \pm 3.4$	$18.5 \pm 0.4$

#### 5.3.2. The application of buffer layer

The variable in the second group is the application of buffer layer (Figure 5.3). Optimized screen printing was employed for all three batches of cells. The first batch of cell did not use any buffer layer, while the second batch adopted 8 nm a-Si:H and the third batch applied 20 nm AZO. All results discussed following are the average value based on 4 cells from the same batch. We firstly compare the value without buffer layer (w/o buffer) to the 8 nm a-Si:H value. The results showed that the efficiency of 8 nm a-Si:H sample decreased by 1.1% like before. The AZO-related results, on the other hand, were unexpected. As discussed in Section 3.7.1, AZO exhibited a better

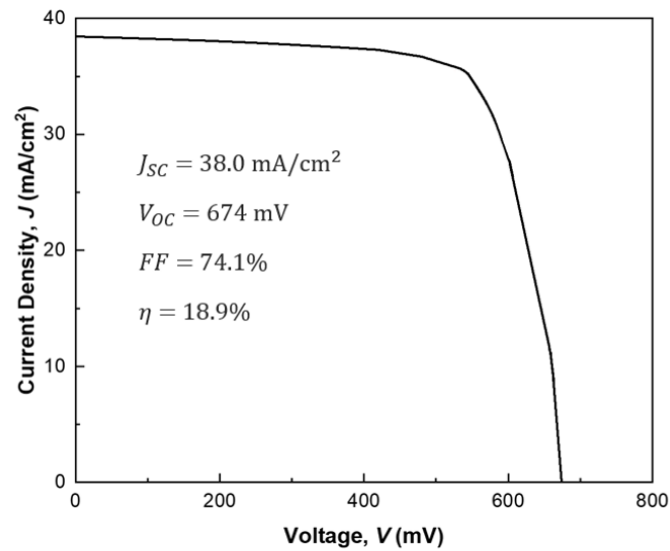


Figure 5.2: The  $J - V$  curve the champion device in this thesis with 18.9% efficiency.

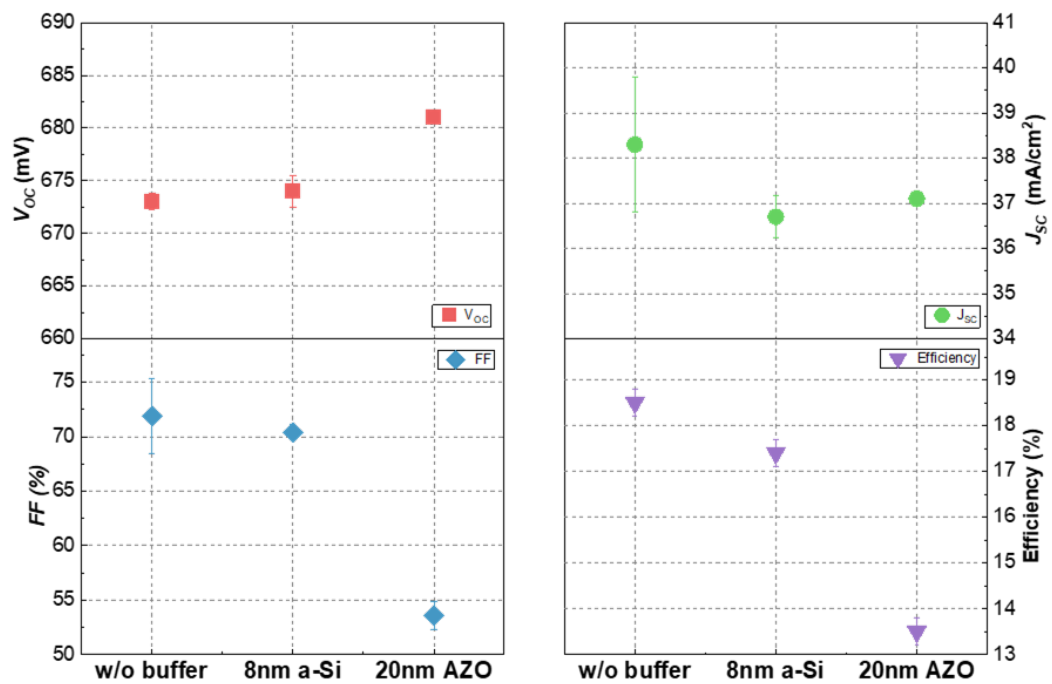


Figure 5.3: The performance of poly-Si(O<sub>x</sub>) cells with/without buffer layer. The values shown are the average based on 4 cells from the same batch.

protective capability as a buffer layer with respect to 8 nm a-Si:H, and hydrogen within the layer could provide additional passivation to the sample. However, although the

$V_{OC}$  of the 20 nm AZO sample indeed increased by 8.0 mV with respect to the w/o buffer, the efficiency was unsatisfactory. Attention was drawn to the 18.3% loss of fill factor. According to the literature, several reasons are proposed[56]. Firstly, the IWO film was not dense enough to prevent the AZO film from strong degradation during high temperature annealing. The usual solution is to deposit additional aluminum oxide as a capping layer after AZO deposition, which is subsequently removed after annealing. This, however, is not feasible for our cell structure. The second possible reason was that during annealing, the hydrogen inside the AZO escaped, resulting in an increase in defect density within the film and a significant decrease in mobility. Another potential reason could be that the AZO was deposited in full area without using any mask. considering the relatively good conductivity of AZO, the unisolated AZO probably led to a small shunt resistance and high shunt losses. All these phenomena led to a dramatic increase in the resistivity of the AZO film, which affected the transport efficiency of the carriers. Ultimately, the cell using AZO as the buffer layer only achieved an efficiency of 13.5%. Among these three cells, the cell without any buffer provided the best performance.

Overall, the cell employing the optimized-SP and without any buffer layer achieved the highest efficiency, 18.9%, which was the champion cell in this thesis. And the average efficiency of this batch cells was 18.5%.

# 6

## Conclusions and outlook

### 6.1. Conclusions

This thesis focuses on poly – Si(O<sub>x</sub>) cells consisting of SiO<sub>x</sub>/poly – Si(O<sub>x</sub>) passivating contact. It is preferred to have thin poly – Si(O<sub>x</sub>) layer because thicker layer will cause remarkable parasitic absorption at the device level. An additional layer of TCO is required to compensate for the high resistance associated with thinner poly – Si(O<sub>x</sub>), but this would introduce passivation degradation. At the same time, the existing screen printing in the lab introduces significant shading losses, therefore a screen printing process capable of printing finer grid lines that bring less shading losses would be beneficial. Based on these aspects, this project has explored methods for passivation degradation mitigation and screen printing optimization.

First, the approaches to reduce the passivation degradation due to IWO deposition were explored. The IWO recipe was optimized to 1.23 W/cm<sup>2</sup> and a gas pressure of 5×10<sup>-5</sup> mbar.  $iV_{OC}$  degradation was 4.7 mV for  $n^+$  and 7.9 mV for  $p^+$  passivation samples (NAOS SiO<sub>x</sub>) after deposition of 75 nm IWO. In particular, different thicknesses of hydrogenated amorphous silicon were tested as buffer layers for the  $p^+$  samples, finding that even a 2 nm hydrogenated amorphous silicon layer was effective in reducing sputtering damage. Then, the optimal post-annealing condition was investigated, which turned out to be vacuum annealing at 400 °C for 30 min. Based on the above results, the first cells were fabricated where  $p^+$  poly – Si(O<sub>x</sub>) was in front and  $n^+$  poly – Si(O<sub>x</sub>) was at the rear. It was found that the optimized-IWO could substantially improve the fill factor and consequently the efficiency compared to the reference IWO recipe. The a-Si:H as buffer was not ideal for poly – Si(O<sub>x</sub>) cells because it led to additional parasitic absorption and lower  $FF$ . Meanwhile, the single-sided (front side) texturing treatment was discovered to bring the higher efficiency compared with double-sided polishing and double-sided texturing. In this batch, the best efficiency was obtained from a cell applied the optimized-IWO, 8 nm a-Si:H as a buffer layer, and

single-sided texturing, at 17.4%. The AZO obtained by ALD was also tested as a buffer layer.

Second, the present screen printing process in the lab was optimized. A screen with 40  $\mu\text{m}$  grid opening width was designed instead of the previous 70  $\mu\text{m}$  grid opening width which aimed to reduce the shading loss caused by metal electrodes. The effect of snap-off distance and squeegee speed on the printing quality was also studied and the optimum values were found to be 0.02 mm and 30 mm/s. Under these conditions, the grid lines painted by the 40  $\mu\text{m}$  opening width screen had a three-dimensional shape and good continuity, and the silver paste widening width was the narrowest at 57.3  $\mu\text{m}$ .

Finally, the poly – Si(O<sub>x</sub>) cells were prepared by applying the above various optimized conditions. Textured  $n^+$  poly – Si(O<sub>x</sub>) was placed on the front side and polished  $p^+$  poly – Si(O<sub>x</sub>) on the rear side. The cell applied optimized-IWO, without any buffer layer and using the optimized screen printing process performed best with an efficiency of 18.9%.

## 6.2. Outlook

There are still some ideas that have not been tried due to experimental equipment malfunction and time constraints. Here, the possible ways to further improve the efficiency of the cell are summarized in the hope of providing some inspiration for future research.

### 6.2.1. TCO-related improvements

- O<sub>2</sub> fraction optimization for IWO

We tried to add oxygen at different fractions in the IWO recipe to reduce the parasitic absorption of IWO and improve the optical performance of the cell. The carrier concentration ( $N_e$ ) and electron mobility ( $\mu_e$ ) after vacuum annealing showed different trends with the O<sub>2</sub> fraction increase, as indicated in Figure 6.2.1.  $N_e$  after annealing decreased monotonically from fraction = 0% to fraction = 0.50% due to the decreasing oxygen vacancy ( $V_O$ ) density caused by the stronger oxygen doping[57]. On the other hand, the mobility remained essentially unchanged, which can be explained by the fact that point defect scattering became weaker while grain boundary scattering grew stronger, and the two effects canceled each other out. Overall, when more than 0.5% oxygen was added, its  $N_e$  is reduced to  $2 \times 10^{20} \text{ cm}^{-3}$  and the  $\mu_e$  remains essentially constant ( $\sim 50 \text{ cm}^2/\text{Vs}$ ), making the resistivity still in the order of  $10^{-4} \Omega \text{ cm}$ . In this way, free carrier absorption was suppressed, but the resistivity did not rise greatly, benefiting the performance of

the solar cell.

The result above certified that the addition of oxygen to the IWO recipe is effective in improving the optical properties of IWO while ensuring its mobility remains unaffected. However, subsequent experiments were suspended due to the temporary inability of sputtering equipment (Zorro in our lab) to incorporate oxygen. It is interesting to verify whether the addition of oxygen to IWO will have an impact on sputtering damage, as well as to explore its influence on the cell.

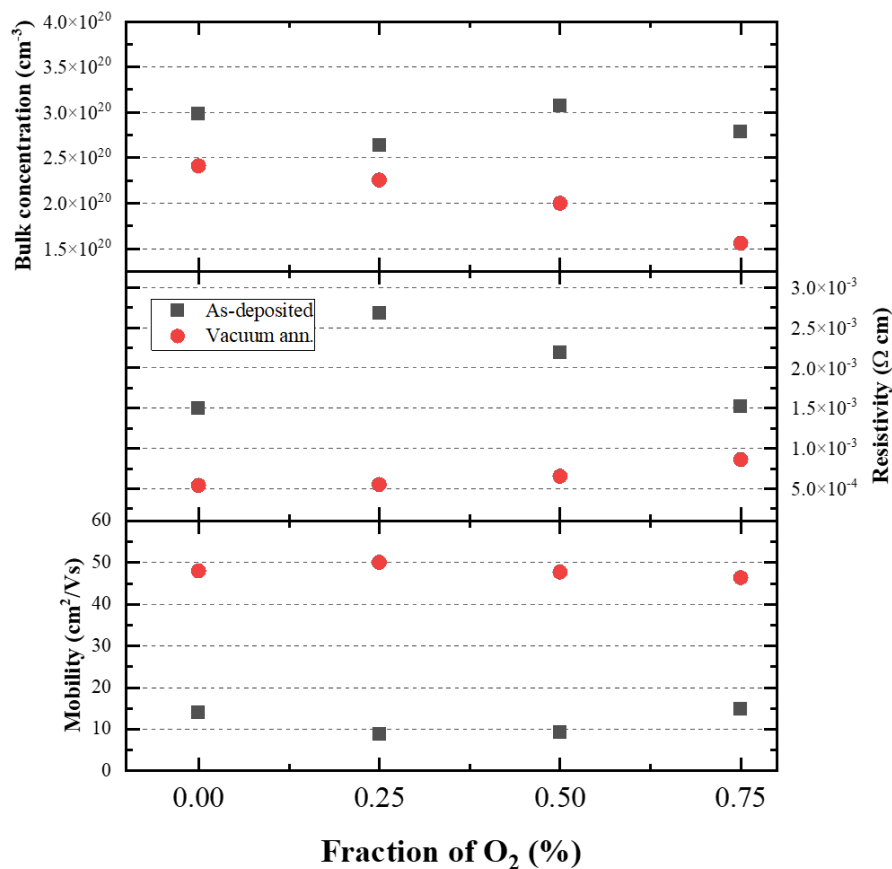


Figure 6.1: The properties of IWO films prepared under various O<sub>2</sub> fraction.

- AZO as buffer layer

As mentioned in Section 5.3.2, the application of AZO obtained by spatial ALD to our cells was not as satisfactory as expected. The possible reason could be that no additional aluminum oxide was deposited as the capping layer of AZO, which led to the degradation of AZO during high temperature annealing. It might be possible to avoid the degradation of AZO if the denseness of IWO is enhanced to

serve as a conductive layer as well as a capping layer.

### 6.2.2. Utilization of copper-plating technique

The metallization method used in this work was screen printing. Although the width of the grids was controlled to  $60\ \mu\text{m}$  or less as far as possible, optical shading loss was still non-negligible. To minimize optical losses and achieve higher short-circuit current density, the metallization can be completed by copper-plating. Copper-plating can further reduce the width of the grids with a uniform shape and good continuity. At the same time the conductivity of copper is almost the same as that of silver, ensuring a good carrier transport[58].

### 6.2.3. Device-related improvements

- TCO-free for rear side

The thickness of poly-Si( $\text{O}_x$ ) on the rear side can be increased appropriately. Since the rear side does not impose as stringent a requirement for parasitic absorption as the front side, thicker poly-Si( $\text{O}_x$ ) can be deposited to achieve the desired electrical properties. In this way, the TCO layer is no longer necessary and its induced passivation damage does not need to be considered.

- Cell edge isolation

Cell edge isolation was not performed during the cell preparation process. This may result in excessive leakage current, low shunt resistance and reduced FF of the cell[59]. Therefore, after metallization is completed, the front and rear surfaces of the cell need to be edge-isolated, which can be accomplished by photolithography[60].

# References

- [1] G. A. Folberth, T. M. Butler, W. J. Collins, S. T. Rumbold, *Environmental Pollution* **2015**, *203*, 235–242.
- [2] C. Kutscher, J. Milford, F. Kreith, *Principles of Sustainable Energy Systems, Third Edition*, CRC Press, **2018**.
- [3] I. E. Agency.
- [4] A. Reinders, *Photovoltaic Solar Energy: From Fundamentals to Applications*, (Eds.: P. Verlinden, W. van Sark, A. Freundlich), Wiley, United States, **2017**.
- [5] A. Smets, K. Jäger, O. Isabella, R. van Swaaij, M. Zeman, *Solar Energy: The physics and engineering of photovoltaic conversion, technologies and systems*, UIT Cambridge Limited, **2016**.
- [6] A. Einstein, *Annalen der Physik* **1905**, *322*, 549–560.
- [7] <https://feng.stafpu.bu.edu.eg/Electrical%20Engineering/2443/crs-14128/Files/Lec%2001%20%282017%29.pdf>.
- [8] T. Markvart, L. Castañer in *McEvoy's Handbook of Photovoltaics*, Elsevier, **2018**, pp. 3–28.
- [9] P. Würfel, U. Würfel, *Physics of solar cells: from basic principles to advanced concepts*, John Wiley & Sons, **2016**.
- [10] Z. Zhao, D. Morel, C. Ferekides, *Thin Solid Films* **2002**, *413*, 203–211.
- [11] J. Benick, B. Hoex, M. Van De Sanden, W. Kessels, O. Schultz, S. W. Glunz, *Applied Physics Letters* **2008**, *92*, 253504.
- [12] J. Melskens, B. W. H. van de Loo, B. Macco, L. E. Black, S. Smit, W. M. M. Kessels, *IEEE Journal of Photovoltaics* **2018**, *8*, 373–388.
- [13] T. G. Allen, J. Bullock, X. Yang, A. Javey, S. De Wolf, *Nature Energy* **2019**, *4*, 914–928.
- [14] J. Melskens, B. W. van de Loo, B. Macco, L. E. Black, S. Smit, W. Kessels, *IEEE Journal of Photovoltaics* **2018**, *8*, 373–388.
- [15] Y. Larionova, H. Schulte-Huxel, B. Min, S. Schäfer, T. Kluge, H. Mehlich, R. Brendel, R. Peibst, *Solar RRL* **2020**, *4*, 2000177.
- [16] E. Aydin, C. Altinkaya, Y. Smirnov, M. A. Yaqin, K. P. Zanoni, A. Paliwal, Y. Firdaus, T. G. Allen, T. D. Anthopoulos, H. J. Bolink, M. Morales-Masis, S. De Wolf, *Matter* **2021**, *4*, 3549–3584.

- [17] Y. Tao, V. Upadhyaya, K. Jones, A. Rohatgi, *AIMS Materials Science* **2016**, *3*, 180–189.
- [18] H. Liu, V. Avrutin, N. Izyumskaya, Ü. Özgür, H. Morkoç, *Superlattices and Microstructures* **2010**, *48*, 458–484.
- [19] Z. Yao, W. Duan, P. Steuter, J. Hüpkes, A. Lambertz, K. Bittkau, M. Pomaska, D. Qiu, K. Qiu, Z. Wu, H. Shen, U. Rau, K. Ding, *Solar RRL* **2021**, *5*, 2000501.
- [20] E. Kobayashi, Y. Watabe, T. Yamamoto, Y. Yamada, *Solar Energy Materials and Solar Cells* **2016**, *149*, 75–80.
- [21] J. E. Swallow, B. A. Williamson, S. Sathasivam, M. Birkett, T. J. Featherstone, P. A. Murgatroyd, H. J. Edwards, Z. W. Lebens-Higgins, D. A. Duncan, M. Farnworth, et al., *Materials Horizons* **2020**, *7*, 236–243.
- [22] J. Yu, J. Bian, W. Duan, Y. Liu, J. Shi, F. Meng, Z. Liu, *Solar Energy Materials and Solar Cells* **2016**, *144*, 359–363.
- [23] I. Hamberg, C. G. Granqvist, *Journal of Applied Physics* **1986**, *60*, R123–R160.
- [24] T. Koida, H. Fujiwara, M. Kondo, *Solar Energy Materials and Solar Cells* **2009**, *93*, 851–854.
- [25] Z. Hu, J. Zhang, X. Chen, S. Ren, Z. Hao, X. Geng, Y. Zhao, *Solar energy materials and solar cells* **2011**, *95*, 2173–2177.
- [26] H. Liu, V. Avrutin, N. Izyumskaya, Ü. Özgür, H. Morkoç, *Superlattices and Microstructures* **2010**, *48*, 458–484.
- [27] R. M. Pasquarelli, D. S. Ginley, R. O’Hayre, *Chem. Soc. Rev.* **2011**, *40*, 5406–5441.
- [28] P. Drude, *Annalen der Physik* **1900**, *306*, 566–613.
- [29] C. Han, L. Mazzearella, Y. Zhao, G. Yang, P. Procel, M. Tijssen, A. Montes, L. Spitaleri, A. Gulino, X. Zhang, O. Isabella, M. Zeman, *ACS Applied Materials & Interfaces* **2019**, *11*, PMID: 31756085, 45586–45595.
- [30] K. Ellmer, T. Welzel, *Journal of Materials Research* **2012**, *27*, 765–779.
- [31] D. Zhang, A. Tavakoliyaraki, Y. Wu, R. Van Swaaij, M. Zeman, *Energy Procedia* **2011**, *8*, 207–213.
- [32] A. H. T. Le, V. A. Dao, D. P. Pham, S. Kim, S. Dutta, C. P. Thi Nguyen, Y. Lee, Y. Kim, J. Yi, *Solar Energy Materials and Solar Cells* **2019**, *192*, 36–43.
- [33] M. Yamada, M. Matsumura, Y. Maeda, *Thin Solid Films* **2011**, *519*, 3352–3357.
- [34] C. Han, PhD thesis, Delft University of Technology, **2022**.
- [35] R. E. Hummel, K. H. Guenther, *Handbook of optical properties: thin films for optical coatings, Vol. 1*, Crc Press, **1995**.
- [36] Z. C. Holman, M. Filipič, A. Descoedres, S. De Wolf, F. Smole, M. Topič, C. Ballif, *Journal of Applied Physics* **2013**, *113*, 013107.

- [37] M. Stodolny, M. Lenes, Y. Wu, G. Janssen, I. Romijn, J. Luchies, L. Geerligs, *Solar Energy Materials and Solar Cells* **2016**, *158*, 24–28.
- [38] Tempress company, <http://www.tempress.nl/company/>.
- [39] P. Babál, **2014**.
- [40] M. Leskelä, M. Ritala, *Thin solid films* **2002**, *409*, 138–146.
- [41] O. Instruments, The mechanism of ALD, [https://plasma.oxinst.com/technology/atomic-layer-deposition?gclid=Cj0KCQjworiXBhDJARIsAMuzAuxp8A0fzkI-RFRsMLrh2Aab60JcGAKbo3vn1gp\\_aMGz7Q9mpeaEsAkaAjFREALw\\_wcB](https://plasma.oxinst.com/technology/atomic-layer-deposition?gclid=Cj0KCQjworiXBhDJARIsAMuzAuxp8A0fzkI-RFRsMLrh2Aab60JcGAKbo3vn1gp_aMGz7Q9mpeaEsAkaAjFREALw_wcB).
- [42] S.-A. company, The difference between classical ALD and spatial ALD. <https://spatialald.com/technology/>.
- [43] R. A. Sinton, A. Cuevas, *Applied Physics Letters* **1996**, *69*, 2510–2512.
- [44] S. Instruments, WCT-120 from Sinton Instruments. <https://www.sintoninstruments.com/products/wct-120>.
- [45] B. Scientific, The DV1 digital viscometer made by Brookfield Ametek, <https://www.viscositeit.nl/viscometers/digitale-viscometer-dv1/>.
- [46] A. Di Gianfrancesco in *Materials for Ultra-Supercritical and Advanced Ultra-Supercritical Power Plants*, (Ed.: A. Di Gianfrancesco), Woodhead Publishing, **2017**, pp. 197–245.
- [47] S. Bradbury, B. J. Ford, D. C. Joy in *Encyclopedia Britannica*, **2019**.
- [48] N. Instruments, Electrons interact with solids to produce different signals. <https://www.nanoscience.com/techniques/scanning-electron-microscopy/>.
- [49] M. Yamada, M. Matsumura, Y. Maeda, *Thin Solid Films* **2011**, *519*, 3352–3357.
- [50] H. Lei, K. Ichikawa, Y. Hoshi, M. Wang, T. Uchida, Y. Sawada, *Thin Solid Films* **2010**, *518*, 2926–2929.
- [51] L. Tutsch, M. Bivour, W. Wolke, M. Hermle, J. Rentsch in Proceedings of the 33rd European PV Solar Energy Conference and Exhibition, **2017**, pp. 24–29.
- [52] T. P. Drüsedau, M. Löhmann, B. Garke, *Journal of Vacuum Science & Technology A: Vacuum Surfaces and Films* **1998**, *16*, 2728–2732.
- [53] C. Hou, MA thesis, Delft University of Technology, **2022**.
- [54] T. Gan, J. Li, L. Wu, J. Zhang, X. Hao, Q. Zhang, R. Li, W. Shi, *Materials Science in Semiconductor Processing* **2022**, *138*, 106257.
- [55] D. E. Riemer, *Microelectronics International: An International Journal* **1989**, *6*, 8–17.
- [56] B. Macco, M. L. van de Poll, B. W. van de Loo, T. M. Broekema, S. B. Basuvalingam, C. A. van Helvoirt, W. J. Berghuis, R. J. Theeuwes, N. Phung, W. M. Kessels, *Solar Energy Materials and Solar Cells* **2022**, *245*, 111869.

- 
- [57] C. Han, Y. Zhao, L. Mazzearella, R. Santbergen, A. Montes, P. Procel, G. Yang, X. Zhang, M. Zeman, O. Isabella, *Solar Energy Materials and Solar Cells* **2021**, 227, 111082.
- [58] G. Limodio, Y. De Groot, G. Van Kuler, L. Mazzearella, Y. Zhao, P. Procel, G. Yang, O. Isabella, M. Zeman, *IEEE Journal of Photovoltaics* **2019**, 10, 372–382.
- [59] I. Hamammu, K. Ibrahim in ICONIP '02. Proceedings of the 9th International Conference on Neural Information Processing. Computational Intelligence for the E-Age (IEEE Cat. No.02EX575), **2002**, pp. 230–232.
- [60] A. Rohatgi, B. Rounsaville, Y.-W. Ok, A. M. Tam, F. Zimbardi, A. D. Upadhyaya, Y. Tao, K. Madani, A. Richter, J. Benick, M. Hermle, *IEEE Journal of Photovoltaics* **2017**, 7, 1236–1243.